University of Central Florida
STARS

Electronic Theses and Dissertations, 2004-2019

2009

Pressure Drop And Endwall Heat Transfer Effects Of Porous Turbulators In A Rectangular Channel

Jared Pent
University of Central Florida

Part of the Mechanical Engineering Commons
Find similar works at: https://stars.library.ucf.edu/etd
University of Central Florida Libraries http://library.ucf.edu

This Masters Thesis (Open Access) is brought to you for free and open access by STARS. It has been accepted for inclusion in Electronic Theses and Dissertations, 2004-2019 by an authorized administrator of STARS. For more information, please contact STARS@ucf.edu.

STARS Citation
Pent, Jared, "Pressure Drop And Endwall Heat Transfer Effects Of Porous Turbulators In A Rectangular Channel" (2009). *Electronic Theses and Dissertations, 2004-2019*. 4104.
https://stars.library.ucf.edu/etd/4104

PRESSURE DROP AND ENDWALL HEAT TRANSFER EFFECTS OF POROUS TURBULATORS IN A RECTANGULAR CHANNEL

by

JARED MATTHEW PENT
B.S. University of Central Florida, 2008

A thesis submitted in partial fulfillment of the requirements
for the degree of Master of Science in Mechanical Engineering
in the Department of Mechanical, Materials, and Aerospace Engineering
in the College of Engineering and Computer Science
at the University of Central Florida
Orlando, Florida

Summer Term
2009

© 2009 Jared M. Pent

ABSTRACT

This study examines the local and averaged endwall heat transfer effects of a staggered array of porous pin fins within a rectangular channel. The porous pin fins were made from aluminum and had a pore density of 10 pores per inch (PPI). The pressure drop through the channel was also determined for several flow rates and presented in terms of the friction factor. Local heat transfer coefficients on the endwall were measured using Thermochromic Liquid Crystal (TLC) sheets recorded with a charge-coupled device (CCD) camera. Static and total pressure measurements were taken at the entrance and exit of the test section to determine the overall pressure drop through the channel and explain the heat transfer trends through the channel. Results are presented for Reynolds numbers between 25000 and 130000 and a blockage ratio (blocked channel area divided by open channel area) of 50%. All results were compared to the corresponding results obtained using solid pins. All experiments were carried out in a 150 mm by 500 mm channel with an X/D of 1.72, a Y/D of 2.0, and a Z/D of 1.72 for the porous pins. It was found that for the range of Reynold's numbers tested in this study, the porous pin array consistently resulted in a larger friction factor, and therefore greater losses than a geometrically similar array of solid pins. The friction factors for the solid pin array were between 9.5 and 10.5, similar to the results found in the literature. For the porous pins, however, the friction factors were significantly increased as the Reynold's number increased, reaching as high as 15.3 at the highest Reynold's number tested. The heat transfer enhancement for the porous pins was found to be between 150 and 170% while the solid pins resulted in a heat transfer enhancement between 190 and 230%.

To my family:

Dad, Mom, Darrell, Christa, Judah, Catie, Gabe, Susanna, Caroline, Evangeline, and Julianna

"Let not the wise man boast in his wisdom…but let him who boasts boast in this, that he understands and knows Me, that I am the Lord…" Jeremiah 9:23

SOLI DEO GLORIA

ACKNOWLEDGMENTS

The author would like to acknowledge the dedicated guidance and assistance of Dr. Jay Kapat. His knowledge and unique approach to learning provided a challenging and rewarding graduate education.

Special thanks go to all the members of the Siemens Energy Center at UCF for their eagerness to provide assistance and advice. Specifically, I would like to thank Mark Ricklick for his knowledgeable assistance in spite of many other responsibilities and Greg Natsui for his diligent help, without which I could not have completed this project.

I would also like to thank my grandparents, Richard and Frances Tobin, for their enthusiastic support and my family for all of their encouragement, criticism, and comic relief.

TABLE OF CONTENTS

LIST OF FIGURES vii
LIST OF TABLES ix
NOMENCLATURE x
CHAPTER 1 – INTRODUCTION 1
Objective of the Present Study 1
Literature Review 3
Experimental Setup 12
Overall Flow Loop 12
Test Section 15
Instrumentation Details 21
Experimental Procedure 26
Data Reduction 28
CHAPTER 2 – TLC CALIBRATION AND HEAT LOSS TESTING 32
Overview of TLC Measurement Method 32
TLC Calibration 33
Heat Loss Testing 34
CHAPTER 3 – RIG VALIDATION 37
Smooth Channel HTC Validation 37
Smooth Channel Friction Factor Validation 38
CHAPTER 4 – EXPERIMENTAL RESULTS AND DISCUSSION 40
Pressure Data and Friction Factor Results 40
Local HTC Data and Results 42
Correction for Lateral Conduction 47
Flow Visualization 49
Averaged HTC Data and Results 53
Enhancement Ratios and Thermal Performance 56
CHAPTER 5 – CONCLUSIONS 60
APPENDIX: COMPUTER CODES FOR TLC PROCESSING 64
LIST OF REFERENCES 77

LIST OF FIGURES

Figure 1: Common Cooling Methods Used in Turbine Blades 2

Figure 2: Array Geometry Tested by Dr. Chyu (1999) 5

Figure 3: Schematic of Test Section Used by Ko et al (2003)..... 7

Figure 4: Schematic of Experimental Setup Used by Ko et al (2003)..... 8

Figure 5: Velocity Vectors for Solid and Porous Baffles at Re = 50000 and *h/H* = 0.5 (Yang et al, 2002) 10

Figure 6: Schematic of Open Flow Loop..... 13

Figure 7: Picture of Actual Rig Used in this Study 14

Figure 8: CAD Drawing of Aluminum Frame Used to Support the Rig..... 15

Figure 9: 3D CAD Model of Test Section..... 16

Figure 10: Picture of Actual Test Section Assembled into the Flow Loop 17

Figure 11: Top View Schematic of Test Section with Pins..... 18

Figure 12: Isometric View of Test Section with Pins..... 19

Figure 13: Sample of Porous and Solid Pins Used in this Study..... 20

Figure 14: Cross-Section View of Test Section with Pins..... 21

Figure 15: Venturi Meter Used to Measure Flow Rate..... 24

Figure 16: Gate Valve and Bleed Valve Connection..... 25

Figure 17: Actual Camera and Lighting Setup 26

Figure 18: Sample of TLC 33

Figure 19: Hue vs. Temperature Calibration Curve..... 34

Figure 20: Heat Loss Curve and Equation..... 35

Figure 21: Smooth Channel HTC Validation 38

Figure 22: Smooth Channel Friction Factor Validation 39

Figure 23: Friction Factor for Solid and Porous Pins 41

Figure 24: Average Endwall HTC's for Solid and Porous Pins Compared to Dittus-Boelter 43

Figure 25: Local HTC Plots for Porous vs. Solid Pins: Re130000..... 44

Figure 26: Local HTC Plots for Porous vs. Solid Pins: Re25000..... 46

Figure 27: Local HTC Plot with Lateral Conduction Correction 48

Figure 28: Flow Visualization Test (Re ~ 5000) 50

Figure 29: Close up View of Flow Visualization 51

Figure 30: Flow Visualization (Porous and Solid) 52

Figure 31: Spanwise Averaged HTC’s for All Cases 54

Figure 32: Spanwise Averaged HTC’s (Re=130000)..... 55

Figure 33: Streamwise Averaged HTC’s (Re=130000) 56

Figure 34: Thermal Performance of Porous and Solid Pins 59

LIST OF TABLES

Table 1: Test Matrix 26

Table 2: Summary of Governing Equations 31

Table 3: Heat Transfer Enhancement Ratios 57

Table 4: Friction Factor Ratios 57

NOMENCLATURE

CCD	= Charge Coupled Device
D	= pin diameter
Dh	= hydraulic diameter (4A/P)
ε	= efficiency
f	= friction factor for blocked channel
fo	= friction factor for open channel
h	= heat transfer coefficient for blocked channel (W/m2K)
ho	= heat transfer coefficient for open channel (W/m2K)
H	= height of channel
HTC	= Heat Transfer Coefficient (W/m2K)
I	= current through heater (amps)
PPI	= pores per inch
q	= heat rate (watts)
R	= heater resistance (ohms)
Re	= Reynolds number
TLC	= Thermochromic Liquid Crystal
V	= voltage
X	= streamwise distance between pins
Y	= spanwise distance between pins
Z	= height of test section

CHAPTER 1 – INTRODUCTION

Objective of the Present Study

In modern gas turbines one of the key ways to increase both the efficiency and power output of the machine is to increase the rotor inlet temperature. This is difficult, however, because the temperature of the fluid flowing through the turbine is already much greater than the melting point of the materials used to make the components of the turbine. As a result, an extensive amount of research is conducted to find ways of cooling critical components inside the turbine, such as the turbine blades and nozzles, and protect them from the hot gases flowing through the machine.

An effective and commonly used method of cooling turbine blades is to incorporate internal cooling passages into the blade. Figure 1 shows some of the common cooling techniques used in turbine blades such as impingement and film cooling, as well as internal cooling. Bleed air from the compressor is forced through these internal passages, drawing heat from the blade by forced convection. Several forms of turbulators are often incorporated into these cooling channels to further increase the heat transfer from the blade into the bleed air. These turbulators often include geometries such as cylindrical shaped pin fins perpendicular to the flow and rectangular shaped ribs or baffles that “trip” the flow as it passes through the cooling channels.

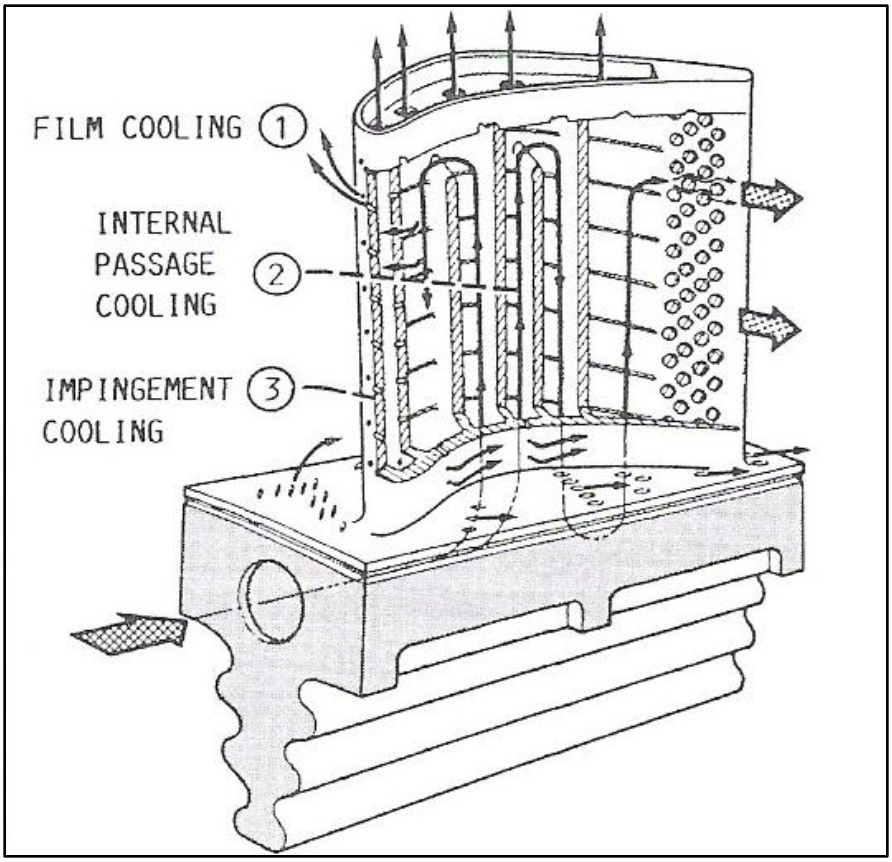

Figure 1: Common Cooling Methods Used in Turbine Blades

The drawback to these methods of increasing the heat transfer from the blade, such as pin fins or baffles, is the resulting pressure from the compressor that is required to push the bleed air through the channels. As the pressure drop between cooling passages increases due to an increased amount of turbulators, the amount of bleed air needed from the compressor also increases, resulting in a decrease in the overall efficiency of the machine. Turbulators can also result in a large variation in the local HTC's, and therefore temperatures, throughout the cooling channel walls due to the formation of wakes behind the turbulators. These large HTC variations

have the potential to create a large amount of thermal stresses in the airfoil material that can lead to component failure.

The purpose of this project was to determine how replacing solid turbulators with porous turbulators changes the flow pattern through the cooling channel as well as the resulting local and average endwall HTC characteristics. There are numerous benefits that could result from replacing solid turbulators with porous turbulators. Because the porous turbulators allow the coolant fluid to partially pass through them, this may result in a significant decrease in the total pressure drop through the cooling channel as compared to solid turbulators. Also, the wakes that are typically formed behind solid turbulators will not be as large behind porous turbulators. This may result in a more even distribution of local endwall HTC's, decreasing the amount of thermal stress on the cooling channel walls.

Literature Review

It has been found that the behavior of the flow around a wall-mounted cylinder significantly impacts the amount of heat transfer from the surface of the wall and cylinder. The boundary layer that typically begins to form over a flat wall becomes broken up by the presence of the pin, creating a flow field around the cylinder base that is commonly referred to as a horseshoe vortex. This horseshoe vortex produces high wall shear stress beneath it, resulting in high heat transfer from the wall in this region (Chyu et al, 1990).

VanFossen (1981) completed work relating to short pin fins, attempting to determine if the data that is commonly available in literature for longer pin fins could be applied to the turbine blade cooling application which implements short pin fins. For his experiments, VanFossen utilized pins that were two diameters long and conducted experiments with Reynold's numbers ranging from 300-60,000. He determined that the heat transfer data for short pins was lower than the available data for longer pins. He also found that the heat transfer from a short pin fin channel was about two times higher than that of an open channel with no pins, even though the wetted surface area can actually decrease from the open channel to the channel with short pins. This is due to the increased turbulence and boundary layer breakup that occurs from the presence of pins in the channel. VanFossen also concluded that the average heat transfer coefficient on the surface of the pins was approximately 35% higher than that of the endwalls.

Chyu et al (1990) used in-line and staggered arrays of pin fins to determine how the array pattern affects the amount of mass transfer from these surfaces, which can be directly correlated to the heat transfer coefficient. Chyu found that that a local maximum and minimum of the normalized Stanton number (a modified Nusselts number) occurs along the symmetry line behind each cylinder in the staggered array. The local maximum occurs at approximately 1 diameter from the pins rear surface and the local minimum occurs at approximately 2 diameters from the pins rear surface. By plotting a spanwise average of the normalized Stanton number, Chyu found that a local maximum occurs immediately ahead of each cylinder in the array. Local maxima of streamwise averaged normalized Stanton numbers were found in regions very close

to the pins. Chyu claimed that these local maxima were a result of the horseshoe vortices that wrap around the cylinder and extend further downstream.

Another study conducted by Chyu (1999) involved arrays of pin fins with a geometry that is considered to be one of the optimal arrangements for turbine blade cooling. This particular geometry included ratios of Y/D and X/D equal to 2.5 and an H/D ratio equal to 1.0. These ratios are commonly used to describe pin-fin geometries and are represented below for a staggered array in Figure 2 (Note that H is the depth of the test section).

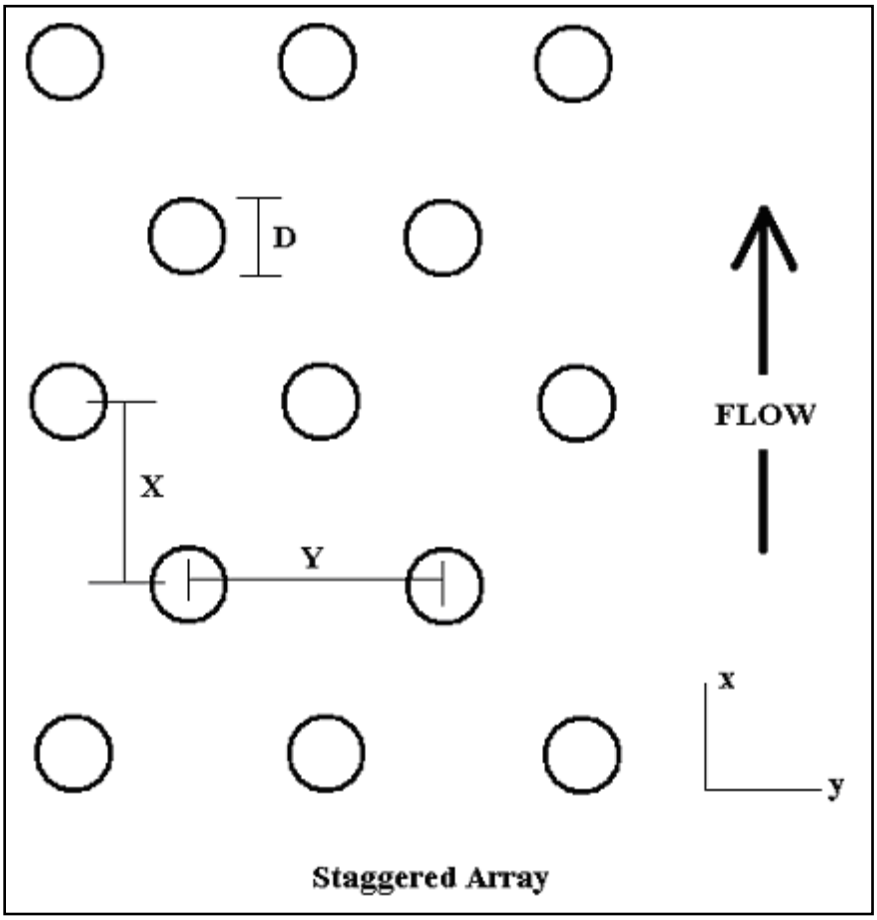

Figure 2: Array Geometry Tested by Dr. Chyu (1999)

In these particular experiments, Chyu tested these arrays for Reynolds numbers varying from 5,000 to 25,000. Chyu found that the column averaged Sherwood number (directly related to Nusselt number) on the surface of the pins was nearly constant across the array span. The row averaged Sherwood number, however, varied significantly along the streamwise direction. For the staggered row, Chyu found that the maximum row averaged Sherwood number occurred at the third row in the array. The enhancement factor, relative to a smooth channel, was found to decrease with increasing Reynolds number. Chyu also determined that the HTC on the pin surface was consistently 10-20 percent higher than that of the endwall.

Ko et al (2003) conducted research with porous aluminum baffles that were mounted on the wall of a heated rectangular channel, one of the few studies that has been done on internal cooling with porous turbulators. HTC's and pressure losses were obtained for different types of porous baffles (varying pore density (PPI) and baffle thickness ratios). Figure 3 shows a schematic of the test section used by Ko.

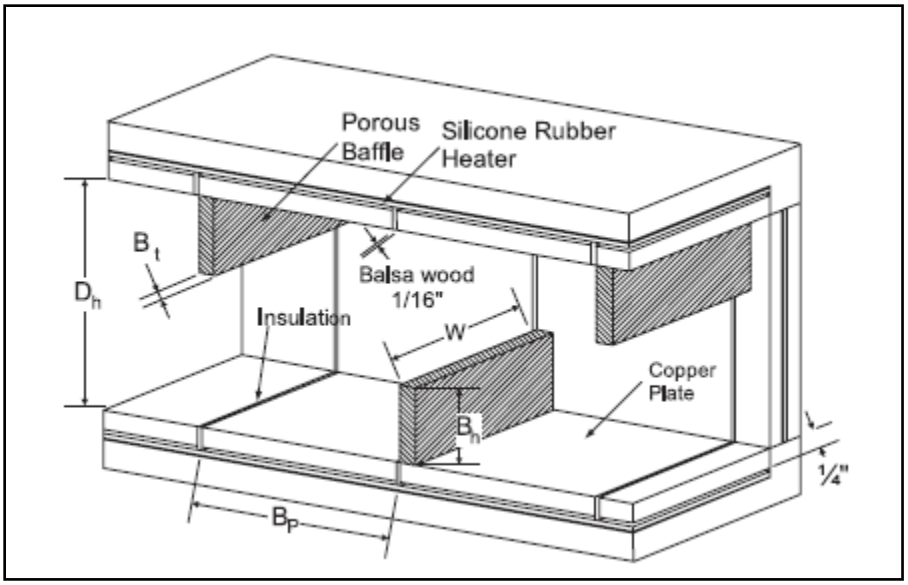

Figure 3: Schematic of Test Section Used by Ko et al (2003)

The test section had a square cross section and was made up of sections of copper plates that were insulated from each other with balsa wood. Thermocouples were placed in each copper section to measure the average temperature of the plates. These different module temperatures were then used to determine the average heat transfer coefficient of each module. Pressure taps were placed at the entrance and exit of the test section to determine the average friction factor through the test section. Figure 4 shows a schematic of the experimental setup used by Ko.

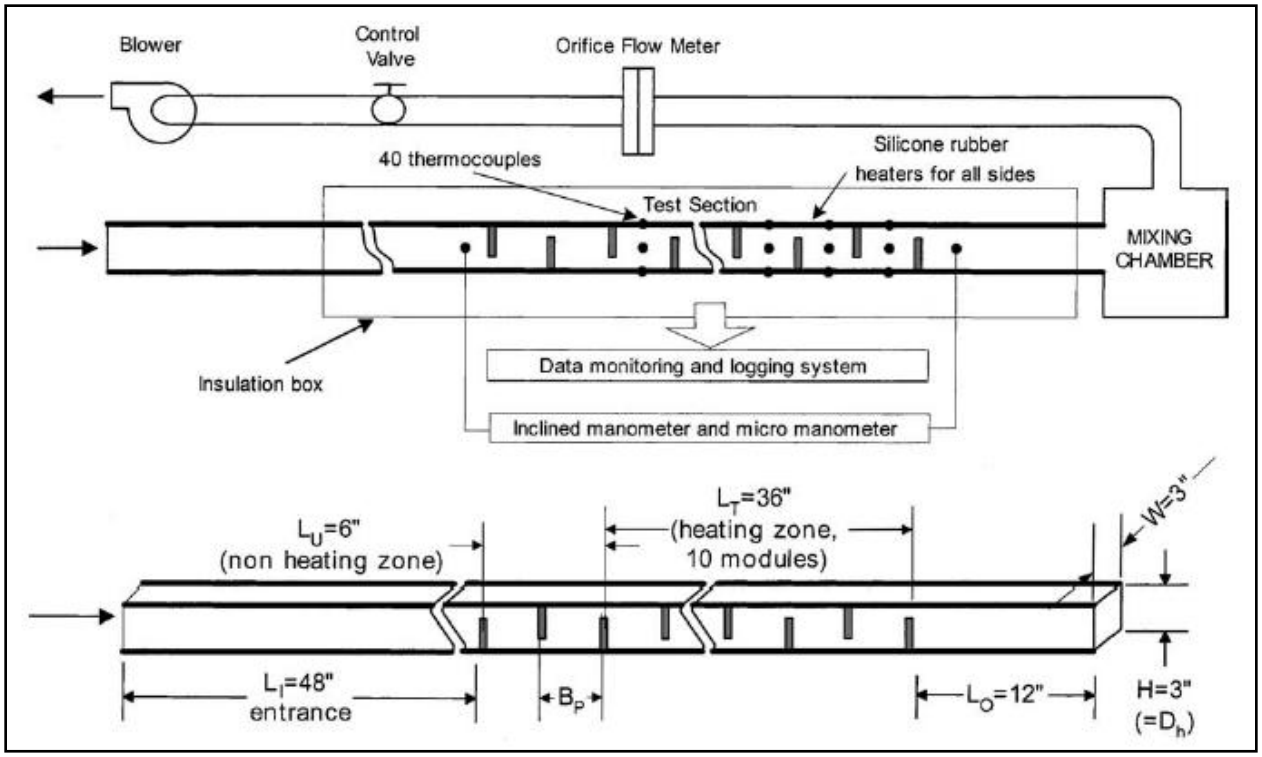

Figure 4: Schematic of Experimental Setup Used by Ko et al (2003)

Ko's tests were run for Reynolds numbers ranging from 20000-50000 and compared to similar tests run with solid baffles. Some of the expected advantages of using porous baffles are a higher surface area to volume ratio, which will increase the dispersion of heat and a forcing of uniform distribution of flow, which will even out the thermal dispersion of the surface, reducing local thermal stress. It was found that the average module Nusselt number decreased in the downstream direction and increased with Reynold's number. The solid baffles performed better than the porous baffles from a heat transfer point of view (enhancement ratio of 390% for solid, 300% for porous). (The enhancement ratio is the ratio of the average module Nusselt number to the Nusselt number in straight channel flow.) The heat transfer enhancement ratio increased with

an increase in pore density. The solid baffles resulted in the greatest friction factor. At constant Reynold's number, the friction factor increased with an increase in pore density. This was concluded to be a result of the increased surface area between the fluid and the solid that occurs with an increase in pore density, thus increasing the amount of hydraulic resistance. It was found that the heat transfer ratio decreased with increasing Reynold's number. This behavior was attributed to the fact that at higher Reynold's numbers the turbulent effects prevail over the enhancement due to porous baffles.

These results found by Ko et al provided some of the basis for the research performed in this study. From a heat transfer point of view, Ko found that the solid baffles performed better than the porous baffles, but only by 30%. Ko also found, however, that the friction factor for the solid baffles was consistently greater than that of porous baffles. For both baffle height to hydraulic diameter ratios tested (1/3 and 2/3), Ko found that the friction factor for the solid baffles was nearly 4 times higher than the friction factor for the porous baffle with the highest pore density. In terms of thermal performance, Ko found that the solid baffles consistently performed better than the porous baffles. At the low B_h/D_h ratio of 1/3, the thermal performance of the solid baffles was only about 4% higher than that of the porous baffles. At the higher B_h/D_h ratio of 2/3, however, the solid baffles performed nearly 30% better than the porous baffles in terms of thermal performance.

Yang et al (2002) performed a numerical study on a channel using both solid and porous baffles with Reynold's numbers between 10,000 and 50,000. One of the main conclusions from this study was that the transport phenomena around the solid and porous baffles were

significantly different. Similar to Ko et al (2003), Yang found that the porous baffled channel possessed a lower friction factor than the solid baffled channel. Yang attributed this to the lower channel blockage that the porous baffles exhibit. Several numerical flow visualization pictures were shown, verifying that the solid baffles resulted in significantly different flow patterns as compared to porous baffles. An example of this is shown below in Figure 5 which shows a figure of the velocity vectors for porous and solid baffles at a Reynold's number of 50,000 and identical baffle height to channel height ratios of 0.5.

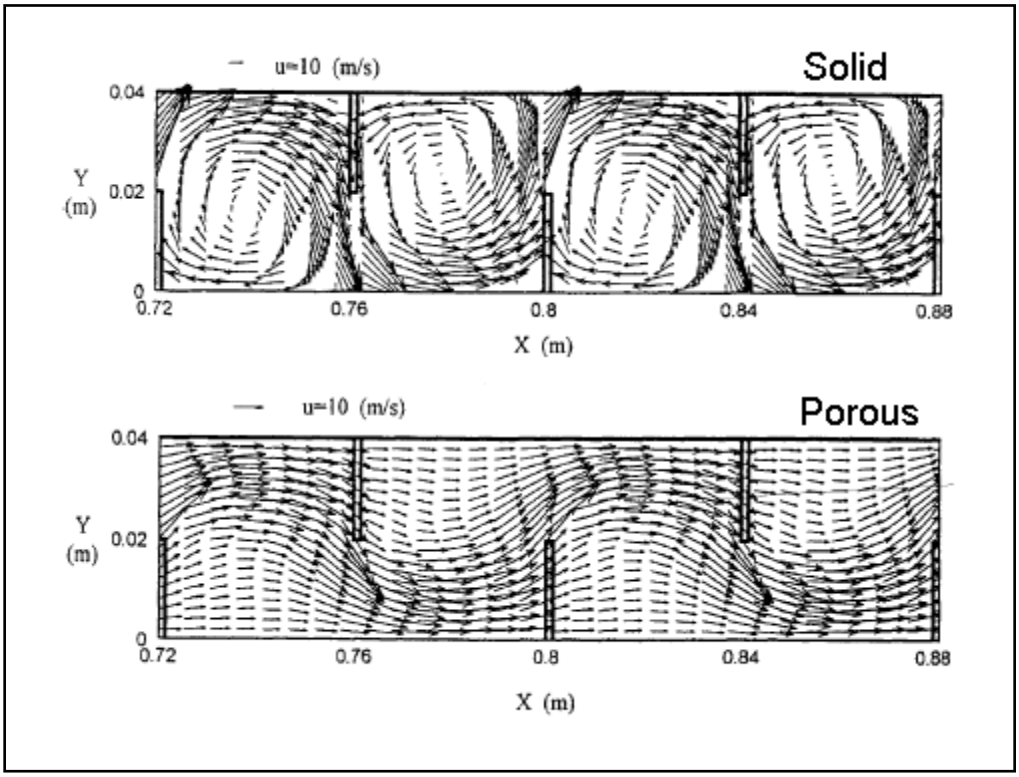

Figure 5: Velocity Vectors for Solid and Porous Baffles at Re = 50000 and *h/H* = 0.5 (Yang et al, 2002)

These flow visualization figures help to confirm what was found by Ko et al (2003), as described earlier. The porous baffles allow a significant amount of the flow to pass through the baffle, therefore reducing the overall friction factor through the channel. It can also be concluded from these results that the temperature distribution on the walls of the channel would be more even for the porous baffled channel, as the flow does not undergo such high recirculation and direct impingement on the channel walls, as is seen with the solid baffles. For this same reason, however, it would be expected that the heat transfer enhancement would indeed be slightly higher for the solid baffled channel as a result of this higher recirculation and direct impingement on the channel walls.

Kim et al (2000) used porous fins made of Al 6101 foam to study their effect in place of louvered fins in a plate fin heat exchanger. Correlations for the friction factor and j-factor were found. 6 fins were used with porosities ranging from 0.89 to 0.96 and pore densities ranging from 10-40 PPI. Reynolds number ranged from ~100-5000. It was found that at low Reynolds numbers, the friction factor of the louvered fin was slightly higher than that of the porous fins. As the Reynolds number increased, however, the porous fins began to have a higher friction factor compared to the louvered fin. The dimensional pressure drop through the test section decreased with an increase in porosity (more pores) but the friction factor increased due to the decreased surface area. The friction factor of the higher permeable porous fin was higher than that of the lower permeable porous fins. As the Reynold's number was increased, the modified j factor decreased and the corresponding convective heat transfer rates, h, increased. The modified

j factor for the porous fins decreased (HTC increased) as the pore density increased or as the porosity decreased.

Although the literature includes good local and average heat transfer data as well as some pressure data, this data is only available for solid pins. While some research has been conducted on porous baffles and ribs, there is little, if any, research on any type of arrays of porous fins. Also, for the research that has been conducted on porous materials, only average data and correlations have been determined. No research has been done that presents local data for the heat transfer characteristics that result from flow through porous materials. The present study focuses on both the local and average endwall HTC's that result from an array of porous pin fins and alternatively wall mounted porous baffles. Local measurements on the endwall will be taken using TLC sheets and pressure data will be taken using a pitot-static probe and pressure taps at the entrance and exit of the test section.

Experimental Setup

Overall Flow Loop

The overall flow loop was an open loop under suction and is shown below in Figure 6. The test section was located in front of the transition piece, allowing the air to enter the PVC exit pipe uniformly and minimize the pressure drop. A PVC pipe was connected to the Venturi Meter, which was used to calculate the flow rate through the test section. A ball valve was used as the primary flow rate bleed valve and a gate valve was used as a secondary flow rate control

valve. The blower was placed at the end of the PVC air line. The PVC pipes and fittings used were all 3 inches in diameter in order to minimize head losses.

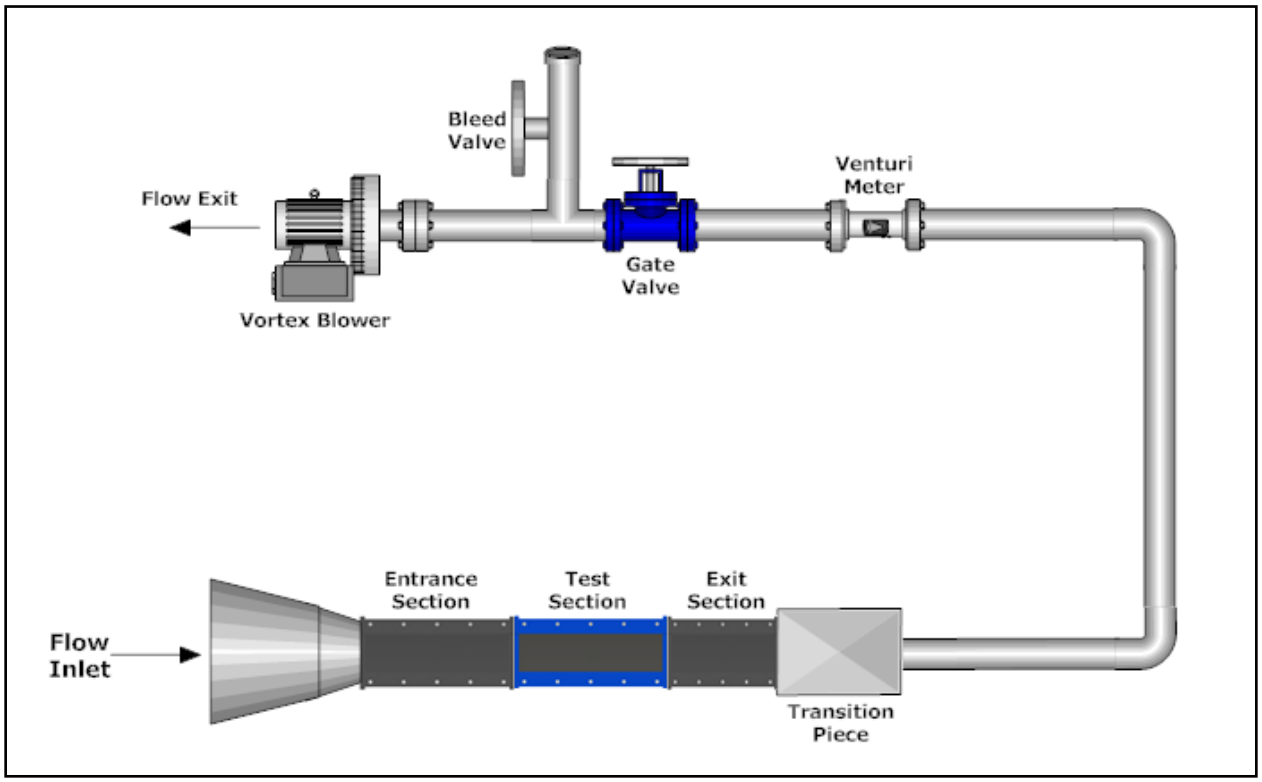

Figure 6: Schematic of Open Flow Loop

Figure 7 shows a figure of the actual rig used in this study, including the entrance and exit sections, the test section, and the transition piece.

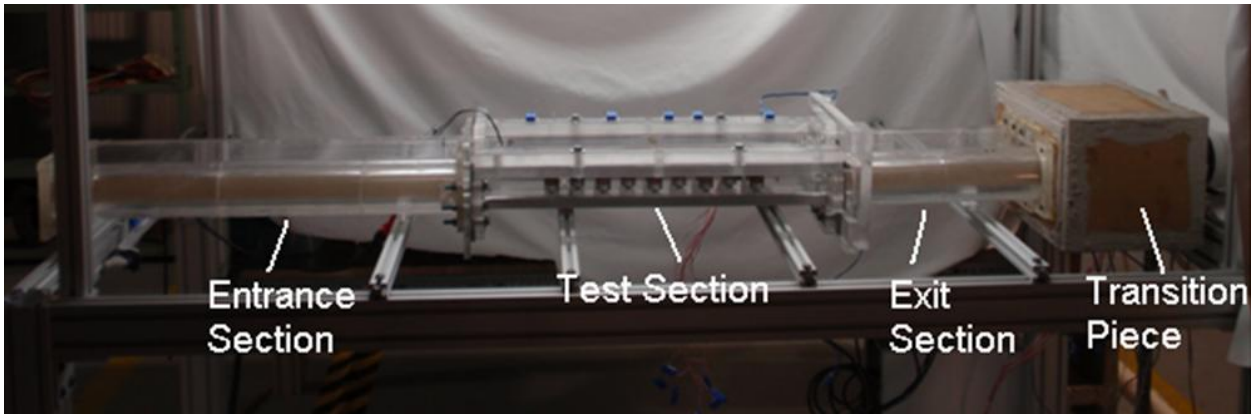

Figure 7: Picture of Actual Rig Used in this Study

The entire rig was mounted on an aluminum frame constructed from 8020 aluminum extrusions. A CAD drawing of this frame is shown below in Figure 8. This frame was also used to mount the fluorescent lights needed to illuminate the test section and included an adjustable camera mount for recording the TLC images.

Figure 8: CAD Drawing of Aluminum Frame Used to Support the Rig

Test Section

The test section, which had a rectangular cross section, was made from ¾" thick acrylic to insulate the experiment from the surroundings and minimize heat loss. Figure 9 shows a 3D CAD model of the test section.

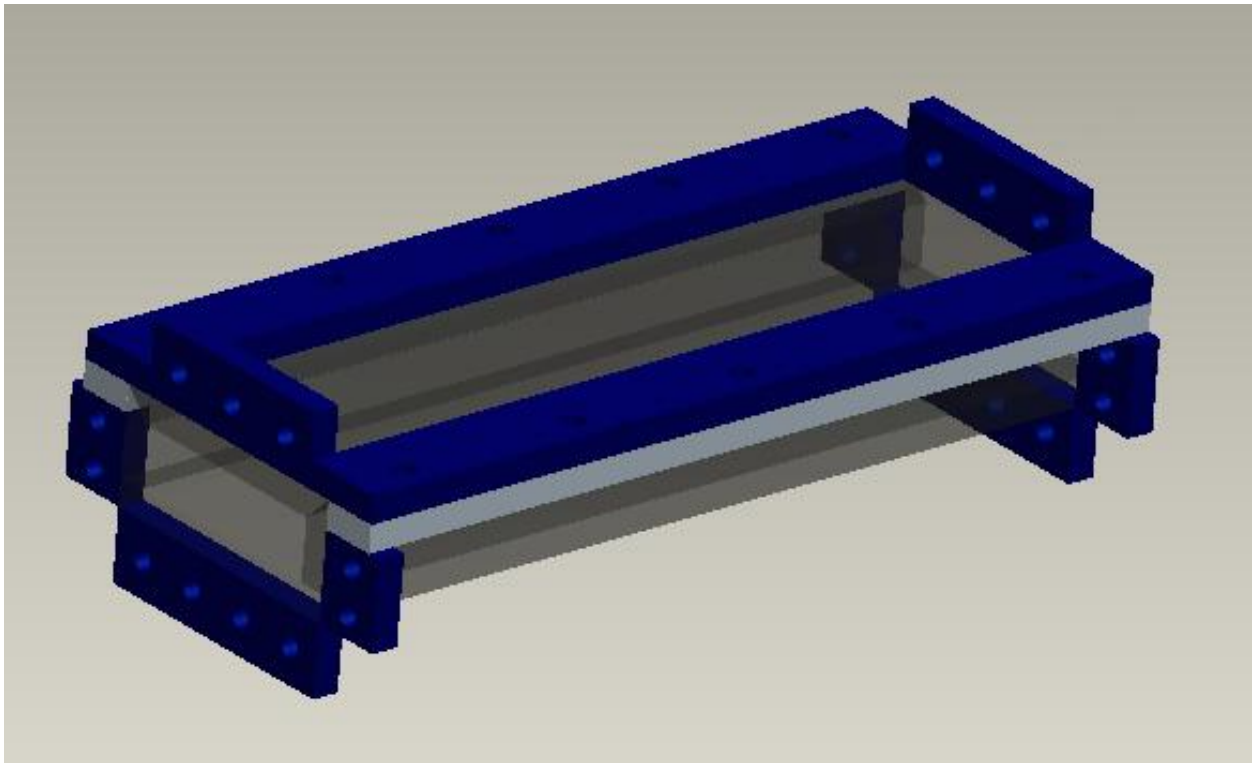

Figure 9: 3D CAD Model of Test Section

Figure 10 shows a picture of the actual test section after complete assembly into the flow loop.

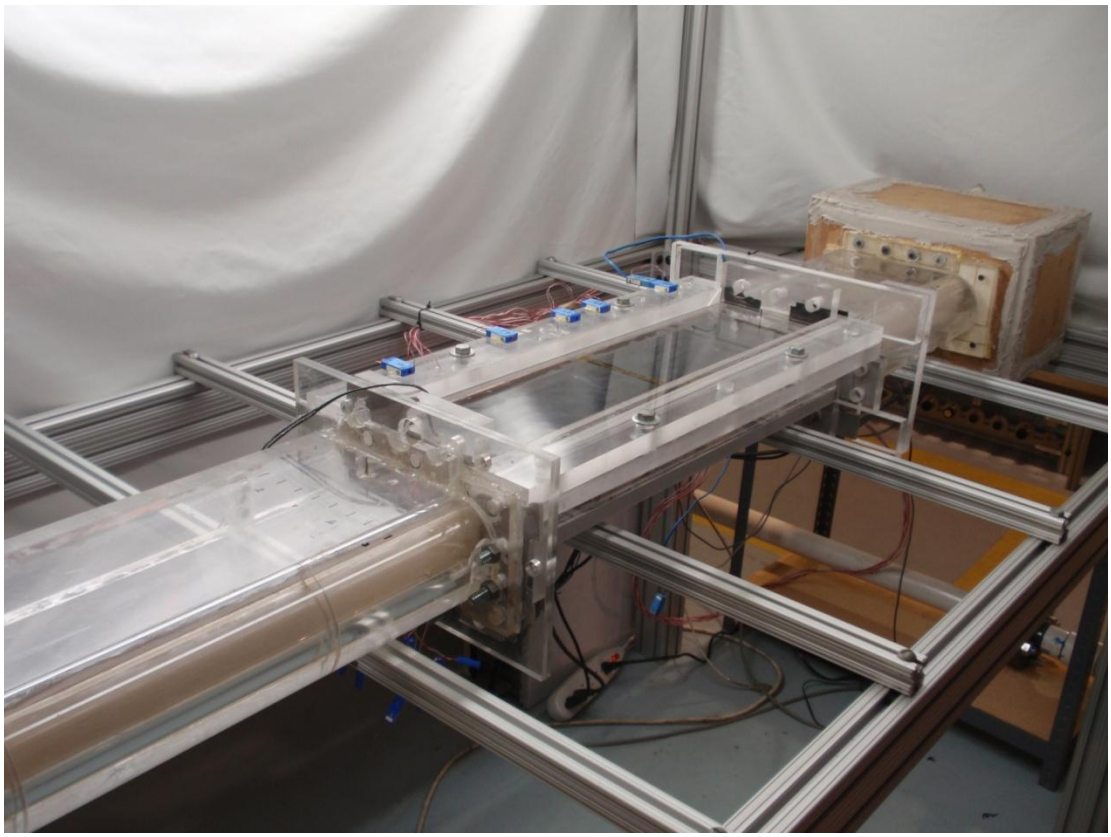

Figure 10: Picture of Actual Test Section Assembled into the Flow Loop

The inside dimensions of the test section were 150mm x 500mm and the inside height of the test section was approximately 43mm. Figure 11 shows a schematic of the top view of the test section with the pin array included. Figure 12 shows an isometric view of the test section.

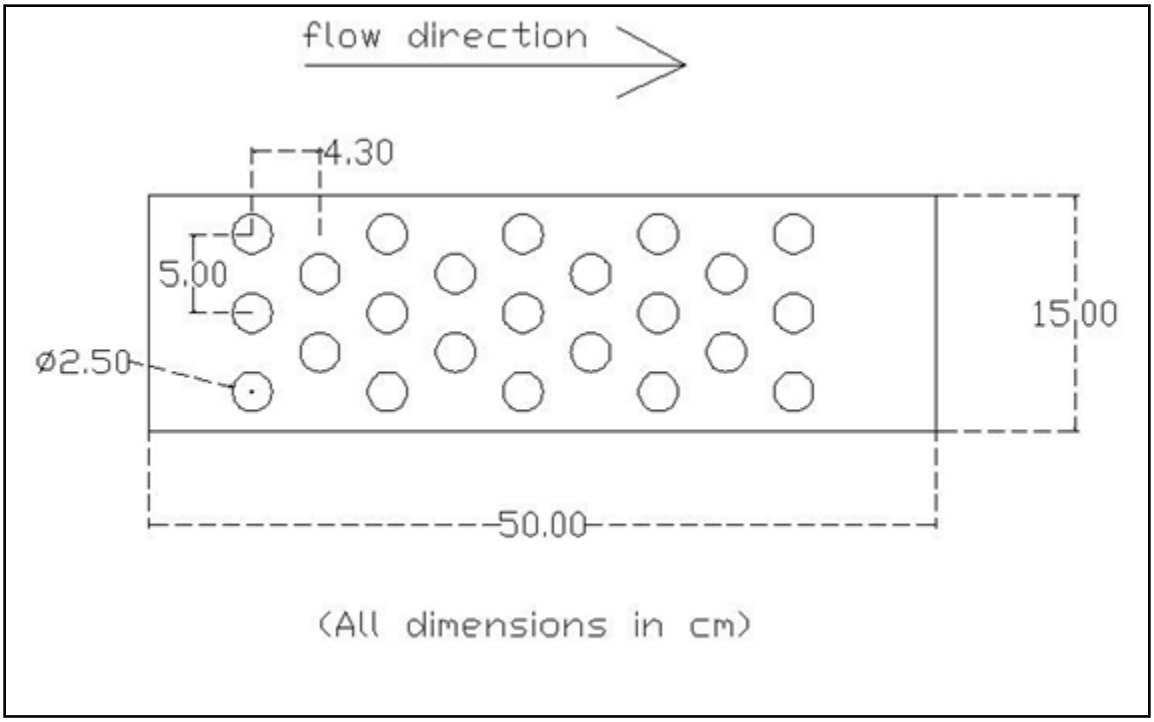

Figure 11: Top View Schematic of Test Section with Pins

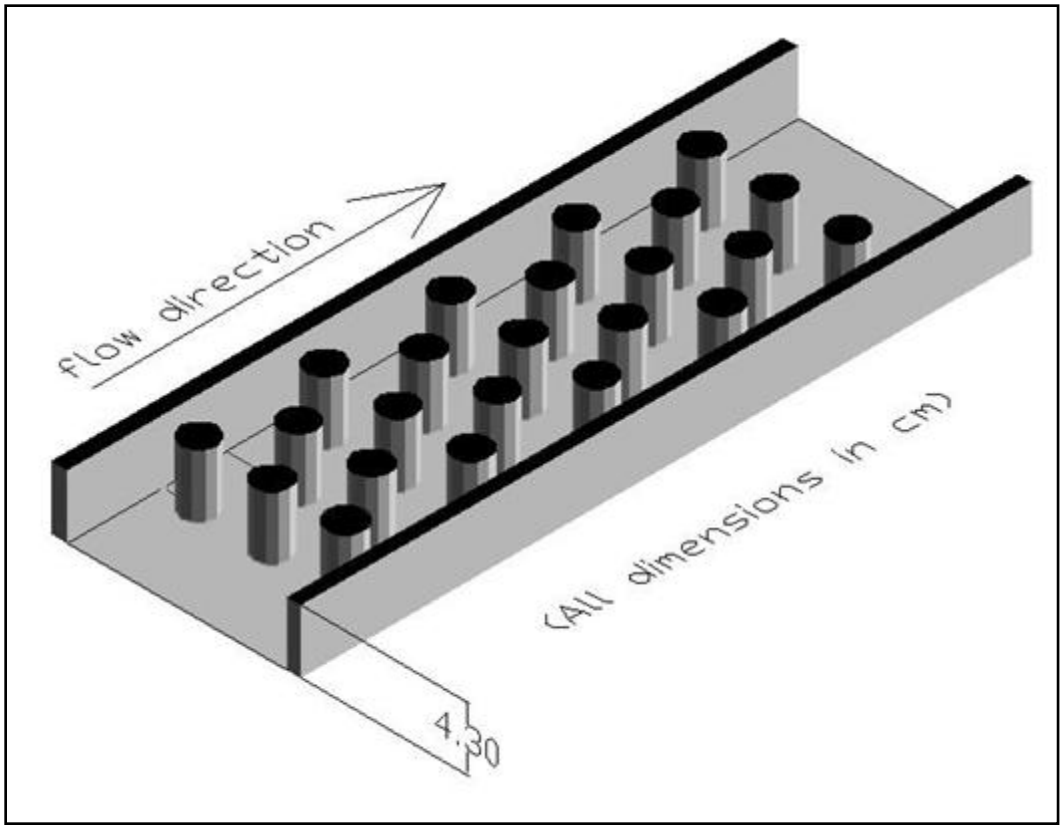

Figure 12: Isometric View of Test Section with Pins

It has been found that the flow through staggered arrays of pins (as in this project) becomes developed after approximately 5 rows of pins (Incropera, 2007). As a result, typical research on pin fin arrays includes up to eight rows of pins in the streamwise direction. Nine rows of pins were used in this project to ensure that the HTC's became developed by the end of the test section. All experiments were carried out with an X/D of 1.72, a Y/D of 2.0, and an H/D of 1.72 so that accurate comparisons could be made with the existing literature.

The cylindrical pins in this study were used to simulate a fin between the top and bottom walls of the test section (endwalls). Both the solid and porous pins had a diameter of 25mm,

corresponding to a blockage ratio of 50%. Figure 13 shows a sample of the actual pins used in this study.

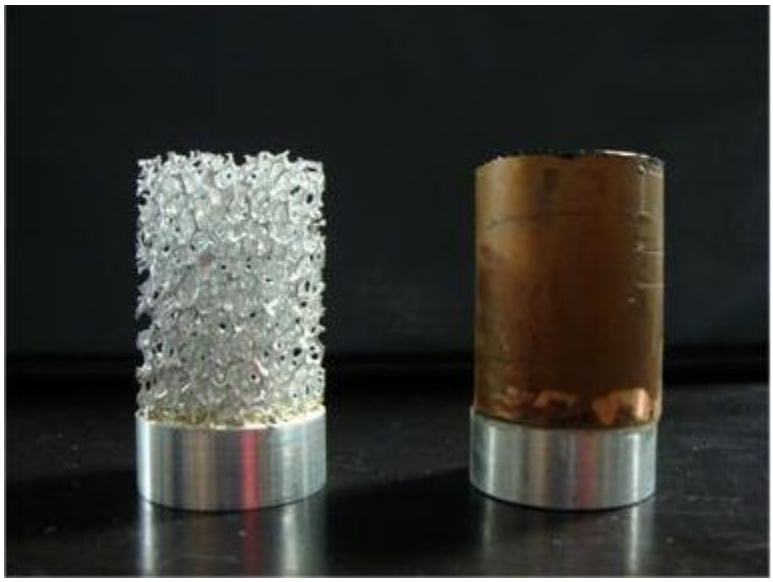

Figure 13: Sample of Porous and Solid Pins Used in this Study

Aluminum disks were bonded to the bottom surface of each pin to provide a removable connection to the bottom endwall of the test section. These disks had a threaded hole drilled through the center so that they could screw onto the studs attached to the bottom of the test section. This allowed for simple replacement of pins as well as minor adjustments in the height of the pin to ensure a good contact between the top of the pin and top endwall.

Instrumentation Details

Figure 14 shows a view of the cross-section of the test section, detailing some of the instrumentation used in this study.

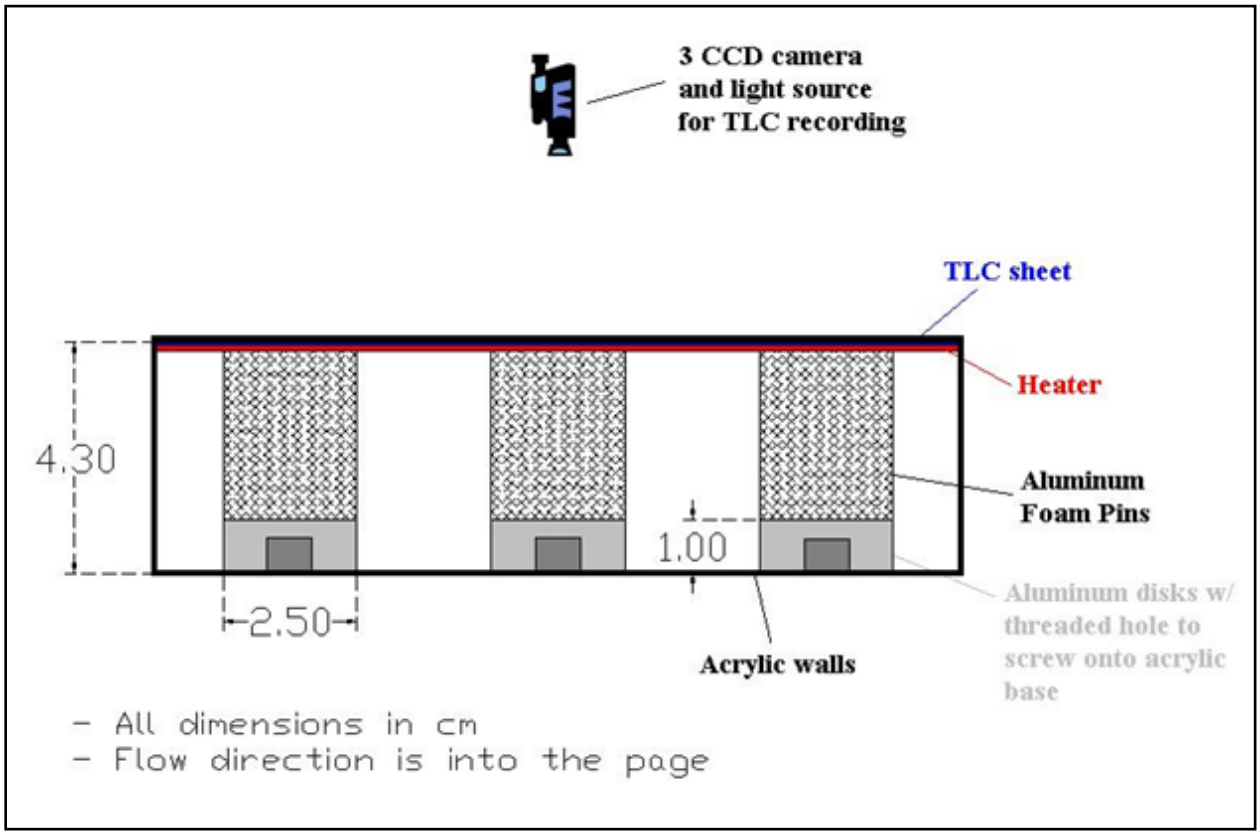

Figure 14: Cross-Section View of Test Section with Pins

Because data was taken from one endwall, it was only necessary to have one wall heater at the top of the test section. A tight connection between the heater and the top surface of the foam pins was important to allow heat to conduct from the heater into the pins.

The heater used in this study was a thin film trace heater, wired in series to a Staco AC Variac transformer (120 Volt, 60 Hz input; 120 Volt, 15 Amp max output). Because the heater was a solid sheet with no geometry variations, the heat flux generated on the endwall surface could be estimated simply by using the known resistance of the heater as well as the known input voltage.

Several thermocouples were placed throughout the test section to verify the data obtained from the TLC. A thermocouple was also placed at the inlet of the test section. All of the thermocouples were of type T. All of the temperature data from the thermocouples was recorded using a data acquisition board (CIO-EXP3) and card (PCIM-DAS16JR/16) along with the LabView computer software. This temperature data was automatically recorded at regular time intervals to ensure that the flow setup had achieved a steady state condition before data recording could begin. The steady state temperatures were then used to verify the data obtained from the TLC.

A sheet of TLC was placed between the heater and acrylic of the top wall and was used to capture the local temperature changes on the endwall of the test section. As temperature changes, the crystals inside the TLC sheets change color and reflect light accordingly. The wide band TLC used in this project had a temperature range between 32 and 52 degrees Celsius. A calibration curve for the camera had to be determined by testing the TLC at each degree within its temperature range. The CCD camera was used to record all video data, which was later converted into image files that could be read and converted into local HTC profiles by the Matlab programs that were developed.

Pressure measurements were taken throughout the test section to obtain the data necessary for friction factor calculations. Two static pressure taps were positioned at the inlet and exit of the test section to measure the pressure drop through the test section. Data from these two pressure taps was taken for each test run during this project. A pitot tube was used to measure the dynamic pressure across the spanwise region of the flow path at the inlet and exit of the test section. Using Bernoulli's equation, this measured dynamic pressure could be used to calculate the velocity of the flow and produce a velocity profile at the inlet and exit of the test section. The cross section of both the entrance and exit sections was divided into a grid for the pitot tube. The pressure measurements were taken at the mid-plane of the test section with six spanwise measurements in that plane. These measurements were used to produce a velocity profile at the inlet and exit of the test section for each test.

A venturi meter was used to measure the flow rate through the test section. It restricts the flow by forcing it through a converging-diverging nozzle and then measures the pressure difference across this restriction. The converging portion of the nozzle causes the flow to accelerate while the diverging portion of the nozzle eliminates any flow separation, allowing for a nearly full recovery of the original pressure head. Using Bernoulli's equation, the flow rate through the test section can be calculated from the pressure difference across the restricted region of the venturi meter. For a more accurate flow rate, an algebraic iteration was used to update the pressure values until they converged within a certain tolerance. Figure 15 shows the venturi meter used in this study.

Figure 15: Venturi Meter Used to Measure Flow Rate

A primary bleed valve and a secondary gate valve were used to control the flow rate through the test section. The bleed valve was used for rough changes in the flow rate and could be used to decrease the flow rate by as much as 50%. The gate valve was used for finer adjustments to the flow rate. Figure 16 shows the gate valve and bleed valve connection used to adjust the flow rate through the test section. A 15 HP three phase blower manufactured by Spencer Turbines was used to generate the suction through the test section and is also partially visible in Figure 16.

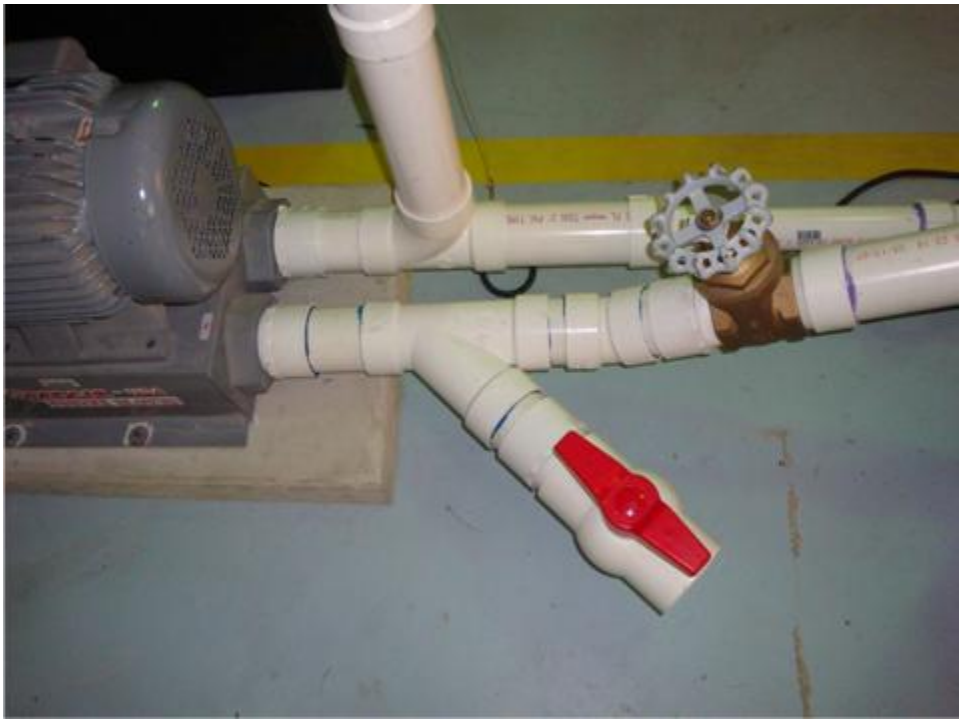

Figure 16: Gate Valve and Bleed Valve Connection

Fluorescent light tubes were used to light the test section. The camera was mounted behind the light source to eliminate shadows. It was important to individually adjust the angle of the camera and lights in order to eliminate glare on the test section surface. Once the lights and camera were initially adjusted it was necessary to keep them in this exact position to eliminate the need for re-calibration. The placement of the camera relative to the test section can be seen in Figure 14, above. A picture of the actual camera and light setup is shown below in Figure 17.

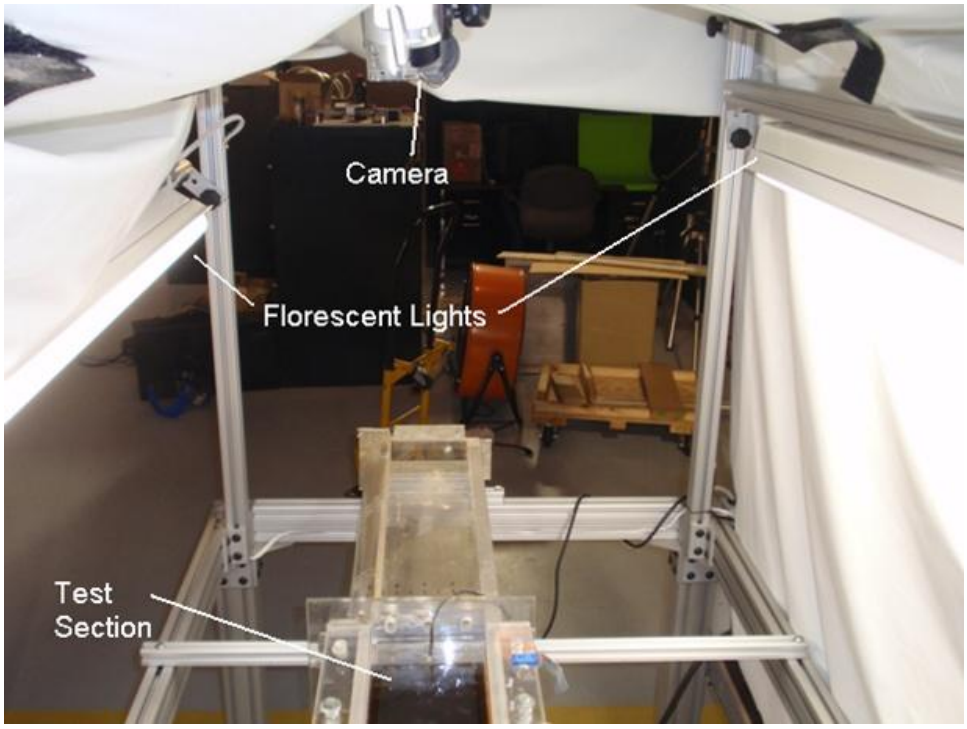

Figure 17: Actual Camera and Lighting Setup

Experimental Procedure

The test matrix for this study, shown in Table 1, included 5 different flow rates for both the solid and porous pins.

Table 1: Test Matrix

Solid Pins	Re 25000	Re 25000	Re 50000	Re 80000	Re130000
Porous Pins	Re 25000	Re 25000	Re 50000	Re 80000	Re130000

Prior to any data measurements, the flow rate through the test section had to be established. The GPM (gallons per min) vs. delta pressure curves, pressure correction, and temperature correction were provided by the venturi meter manufacturer. This data was then

used to achieve the desired flow rate by measuring the pressure change through the venture meter with a manometer and then adjusting the valves, as described earlier.

For an accurate steady state assumption to be achieved, it was necessary to run the blower for at least 30 minutes before any data could be collected. This allowed sufficient time for the blower to achieve its steady running temperature and prevented a decrease in the flow rate that results from an increasing blower temperature. Periodic tests were performed to ensure that the 30 minute warm up time was sufficient to allow the blower to come to steady state.

Once the flow rate through the test section was established, pressure measurements could be taken. This involved using the pitot tube to measure the dynamic pressure inside the entrance and exit sections of the flow loop at several locations, as described above. Using the pitot tube and a manometer, the pressure data was recorded and then input into an Excel spreadsheet. This spreadsheet was then used to average the pressure data and convert it to velocity profiles. The static pressures at the inlet and exit to the test section were also taken and recorded to determine the pressure drop through the test section

The next step in the experimental procedure was to capture the HTC data. As the voltage supplied to the heaters was increased, the thermocouple temperatures were monitored through the LabView program to ensure that none of the temperatures throughout the test section got too hot. The power to the heater was slowly increased until the average temperature of the endwall was approximately 20 degrees C above the ambient temperature. When the desired temperature was achieved, the system was left for up to an hour to achieve a steady state condition. This condition was verified by recording temperatures every several minutes with the DAQ system

and ensuring that the temperatures no longer changed with time. Once a steady state condition was achieved, the image was recorded with the camera for 15-20 seconds after eliminating all outside sources of light.

After recording the TLC image, this video was broken up into 30 frames per second, resulting in approximately 450 separate images. These images were then averaged together to produce one image file. After cropping this image file to the desired region of data, it was read by the Matlab code, pixel by pixel, to develop a matrix of hue values. Each of these hue values were then compared to the TLC calibration curve and converted to a local temperature profile of the endwall. The local temperature profile was then used to create the local HTC profile by using the known heat flux input.

Data Reduction

Before designing the test section and the test rig it was necessary to determine the theory that would be used to analyze the data and the corresponding assumptions that would have to be made.

It was determined that the data would be collected once the setup had reached a steady state condition. This required an initial warm-up period for the blower and heater until the various temperatures throughout the test section no longer varied with time. Because all of the data was collected while the test section was under steady state conditions, the temperature range throughout the test section was relatively wide, varying from approximately 40 – 60 degrees

Celsius. This required the use of wide-band TLC (with a temperature range of 20 degrees C) so that this wide range of temperatures could be captured.

The heater on the endwall was assumed to produce a constant heat flux throughout its surface. This allowed for the generated heat flux to be calculated using Equation (1), knowing the input voltage, the input current, and the heater resistance.

$$Q = \frac{V^2}{R} = I^2 R \tag{1}$$

Thick acrylic was used to make the test sections for two reasons. First it was necessary that the material be clear so that the camera could see through it to record the pictures of the TLC sheet. Secondly, a thick, non-conductive material was needed to minimize the heat loss out of the test section. A separate entrance and exit section with the same interior dimensions as the test section were also used before and after the test section so that the flow was developed before entering the test section and unrestricted after leaving the test section.

The efficiency of each particular test was beneficial in comparing the change in HTC with the change in pressure drop through the test section. While the highest HTC's are achieved for the largest pin size and highest flow rate, this combination also results in the largest pressure drop due to the significant increase in blocked area. Consequently, it is important to produce a comparison between these two factors. Equation (2) was used to determine the efficiency of each test, using the open hydraulic diameter.

$$\varepsilon = \frac{h/h_o}{f/f_o^{1/3}}$$

(2)

An uncertainty analysis was performed to determine the uncertainty of the HTC measurements and the friction factor measurements. Each uncertainty calculation was done using Equation (3), shown below.

$$U_f = \sqrt{\left(u_m \frac{\partial f}{\partial P}\right)^2 + \left(u_\rho \frac{\partial f}{\partial \rho}\right)^2 + \cdots \left(u_c \frac{\partial f}{\partial D_h}\right)^2}$$

(3)

In this uncertainty equation, the lowercase *u*'s represent the measurement uncertainty of each variable needed to calculate a given function. This information is often obtained from the inaccuracies of the various measuring devices provided by the manufacturer. The partial derivatives are taken of the function with respect to each variable in that function. The square root of the sum of the squares of these factors is then taken as the uncertainty of that particular function. It was estimated that the uncertainty of the HTC measurements presented in this study is +/- 12.3% while the estimated uncertainty of the friction factor measurements presented in this study is +/- 9.5%.

A summary of some of the governing equations used in this study is shown below in Table 2.

Table 2: Summary of Governing Equations

Energy Balance	$Q_{in} = \frac{V^2}{R} - Q_{loss} = I^2R - Q_{loss}$
Newton's Law of Cooling	$Q_{in} = hA(T_w - T_\infty)$
Dittus Boelter Correlation	$Nu = 0.023Re^{0.8}Pr^{0.4} = \frac{hk_f}{D_h}$
Blasius Correlation	$f = \frac{0.316}{Re^{0.25}}$
Thermal Performance	$\varepsilon = \frac{h/h_o}{f/f_o^{1/3}}$
Reynold's Number	$Re = \frac{\rho V D_h}{\mu}$
Hydraulic Diameter	$D_h = \frac{4A}{P}$
Uncertainty	$U_f = \sqrt{\left(u_m \frac{\partial f}{\partial P}\right)^2 + \left(u_\rho \frac{\partial f}{\partial \rho}\right)^2 + \cdots \left(u_c \frac{\partial f}{\partial D_h}\right)^2}$

CHAPTER 2 – TLC CALIBRATION AND HEAT LOSS TESTING

Overview of TLC Measurement Method

The bandwidth of a TLC crystal is defined as the temperature limit that begins at a minimum activation temperature and ends at a clearing point where the TLC will no longer reflect color. A pure thermochromic liquid crystal that is within its bandwidth of temperatures will reflect a unique color of visible light when illuminated by white light. Because this behavior is repeatable and reversible, it allows the TLC color to be directly calibrated as a function of temperature only (Farino, 1994). However, the unique color of visible light that each crystal reflects is also a function of the background lighting and the viewing angle. It is therefore important to ensure that the intensity and position of the background lighting as well as the location of the camera does not change once the calibration data is recorded.

The thermochromic liquid crystals can be encapsulated and suspended in a sprayable material or applied to an adhesive sheet. For this study, the adhesive sheet type was used for all experiments and was obtained from Liquid Crystal Resources. Figure 18 shows a sample TLC sheet which is showing the difference in temperature between a hot laptop surface and a cool desk surface.

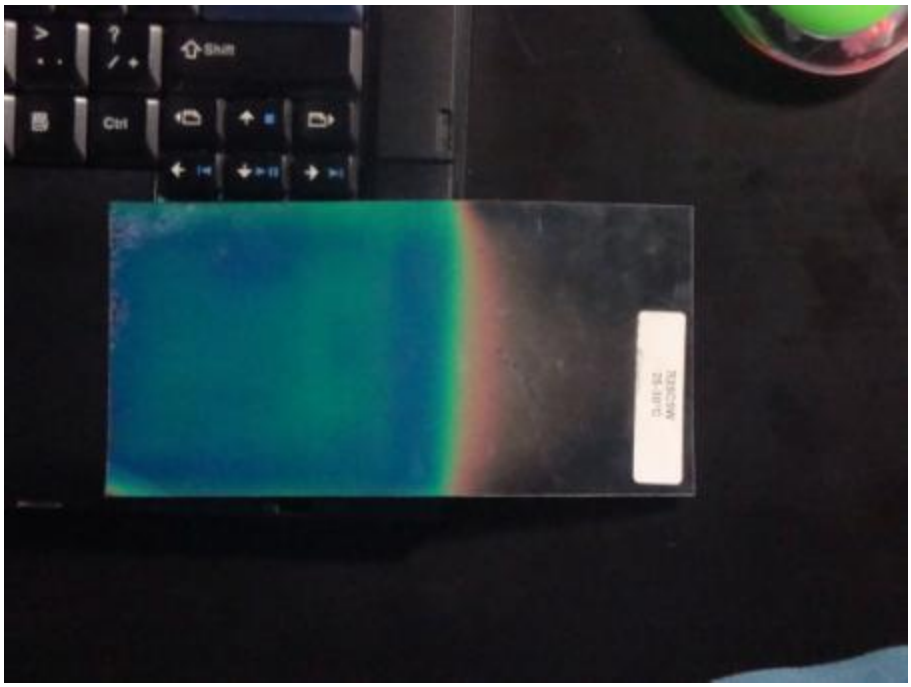

Figure 18: Sample of TLC

TLC Calibration

The first step in the TLC calibration process was to warm up the heater (with no flow through the test section) until it was just above the maximum temperature of the TLC. For the TLC used in this study, this maximum temperature was visible when the TLC turned from dark blue back to black. Once this maximum temperature was achieved, the heater was turned off. The camera recording and the temperature recording (with the DAQ) were then begun simultaneously to ensure that each temperature measurement could be matched with its corresponding image from the camera. Using this data, a snapshot was taken for each degree change from approximately 30-60 degrees Celsius. Each of these snapshots were then read using a Matlab code that determined the hue value of the TLC at each particular temperature. This hue

vs. temperature data could then be plotted and a calibration curve developed. The TLC calibration curve as well as the calibration equation for this study is shown in Figure 19.

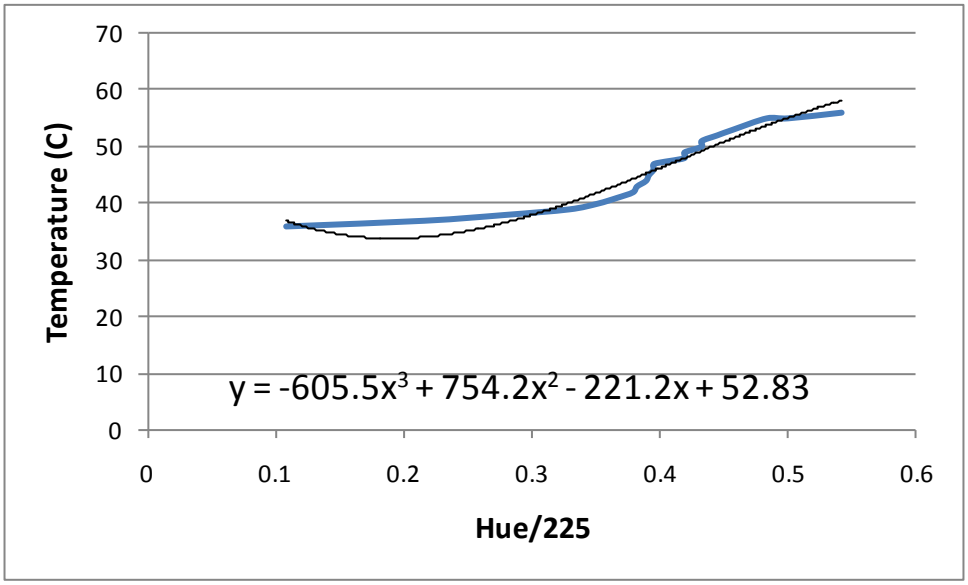

Figure 19: Hue vs. Temperature Calibration Curve

The equation developed from this calibration data was then incorporated into the Matlab code that read the hue of each pixel in a given data image and converted it to a temperature value using this calibration curve.

Heat Loss Testing

In order to achieve accurate results, it was necessary to determine the heat loss out of the test section. Several heat leakage tests were run to determine how much heat was lost through the walls of the test section. During the heat leakage testing, the blower remained off and the inside

of the test section was filled with insulation. This prevented any heat transfer to the inside of the test section and only allowed for conduction from the heater into the acrylic and finally to the surrounding air. With low supplied power to the heater, the heat loss could be determined knowing the temperature data from the wall surface, the temperature of the surrounding air, the thermal conductivity of the materials, and the natural heat transfer coefficient of air. Using these measurements, taken at two different input powers, a curve was developed that related the heat loss to the supplied power to the heater, or the average temperature of the heater. This relation is shown below in Figure 20.

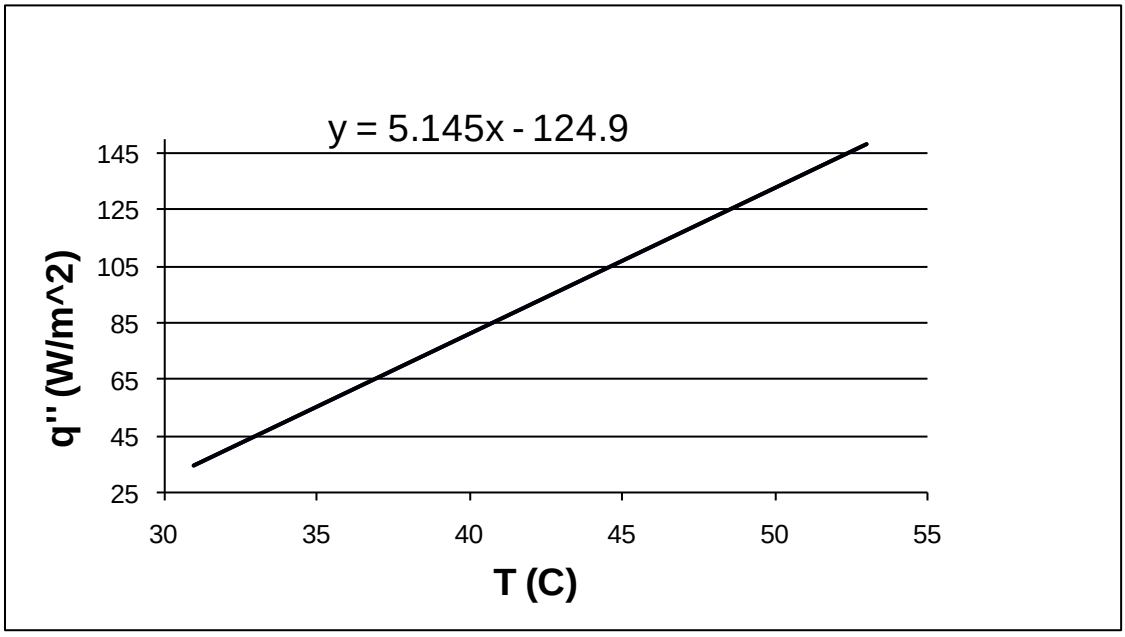

Figure 20: Heat Loss Curve and Equation

This equation could then be incorporated into the Matlab code that was used to determine the values of the local HTC's through the endwall. Knowing the average temperature of the heater,

the heat loss could be calculated from the developed equation and was then subtracted from the overall known heat input. This resulted in an accurate calculation of the actual supplied heat flux to the endwall surface.

CHAPTER 3 – RIG VALIDATION

To validate the results found in this project it was necessary to run a validation setup that could be compared against known data. This validation was done by removing the pins from the test section and covering the studs with a flat plate. Flat plates with the same thickness were also placed at the bottom of the entrance and exit sections so that a smooth rectangular channel was made. The HTC and pressure drop results for this smooth channel were then compared to the Dittus Boelter correlation and the Blasius correlation, respectively.

Smooth Channel HTC Validation

For the HTC validation, tests were run at Reynolds numbers of approximately 30000, 130000, and 193000. Using a region of the TLC data from the developed region of the test section, an average HTC value could be calculated along the wall of the smooth channel and compared with the Dittus Boelter correlation for turbulent flow in smooth channels. Figure 21 shows the results for the HTC validation.

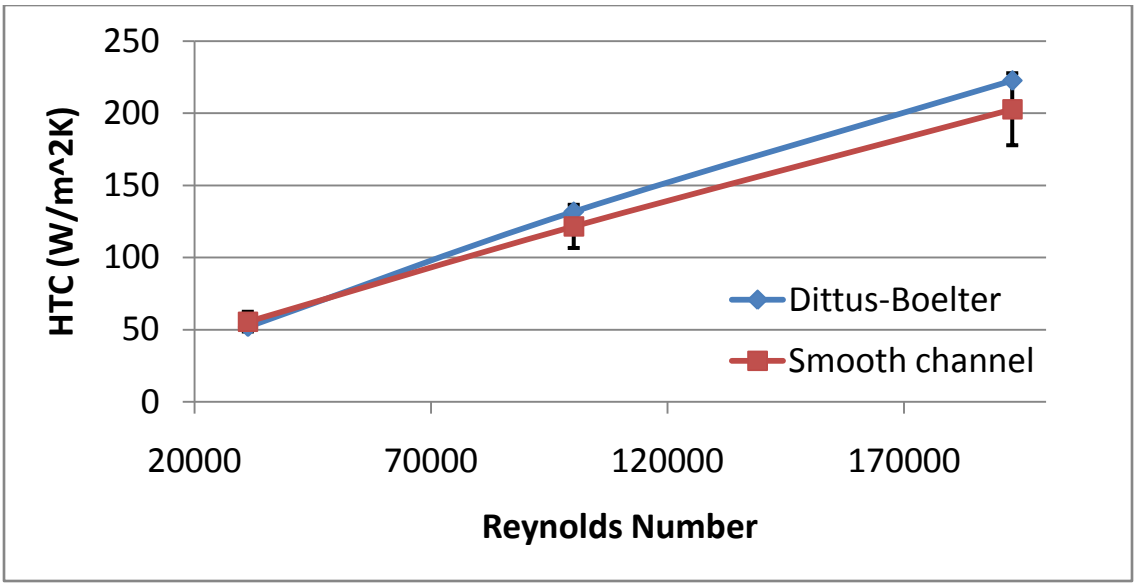

Figure 21: Smooth Channel HTC Validation

From the figure it is evident that the measurement methods used in this project result in average HTC values that are very close to the known analytical results over a wide range of Reynolds numbers. It is apparent that as the Reynold's number is increased, the deviation from the analytical results slightly increases, however, for a Reynold's number of nearly 200,000, the deviation from the Dittus Boelter correlation is still less than 9%. Also, notice from the figure that for the range of Reynold's numbers used in this project (< 150000), the experimental setup produced results that were within 7% of the analytical results.

Smooth Channel Friction Factor Validation

Static pressure measurements were also taken during the validation runs and were used to calculate the friction factor through the smooth channel. This was then compared to the Blasius

correlation for the friction factor for turbulent flow in smooth pipes. Figure 22 shows the results for the friction factor correlation.

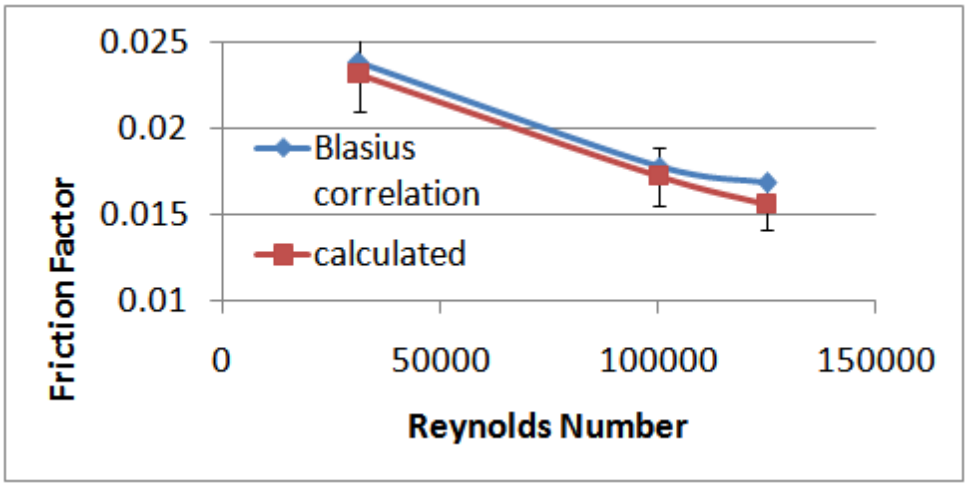

Figure 22: Smooth Channel Friction Factor Validation

CHAPTER 4 – EXPERIMENTAL RESULTS AND DISCUSSION

Pressure Data and Friction Factor Results

Pressure and heat transfer results were obtained for solid and porous pins at Reynold's numbers between 25,000 and 130,000. To obtain the friction factor through the test section, it was necessary to measure the static pressure at the entrance and exit of the test section. The average velocity through the test section was determined by measuring the dynamic pressure at several locations along the exit plane of the test section using a pitot-static tube. Using the static pressure drop and the average velocity through the test section, a friction factor through the test section could be determined and compared to the Blasius correlation through a smooth channel. Figure 23 shows a plot of the friction factors vs. Reynold's number for 5 different flow rates using porous and solid pins. The figure also includes correlations for the data that was obtained.

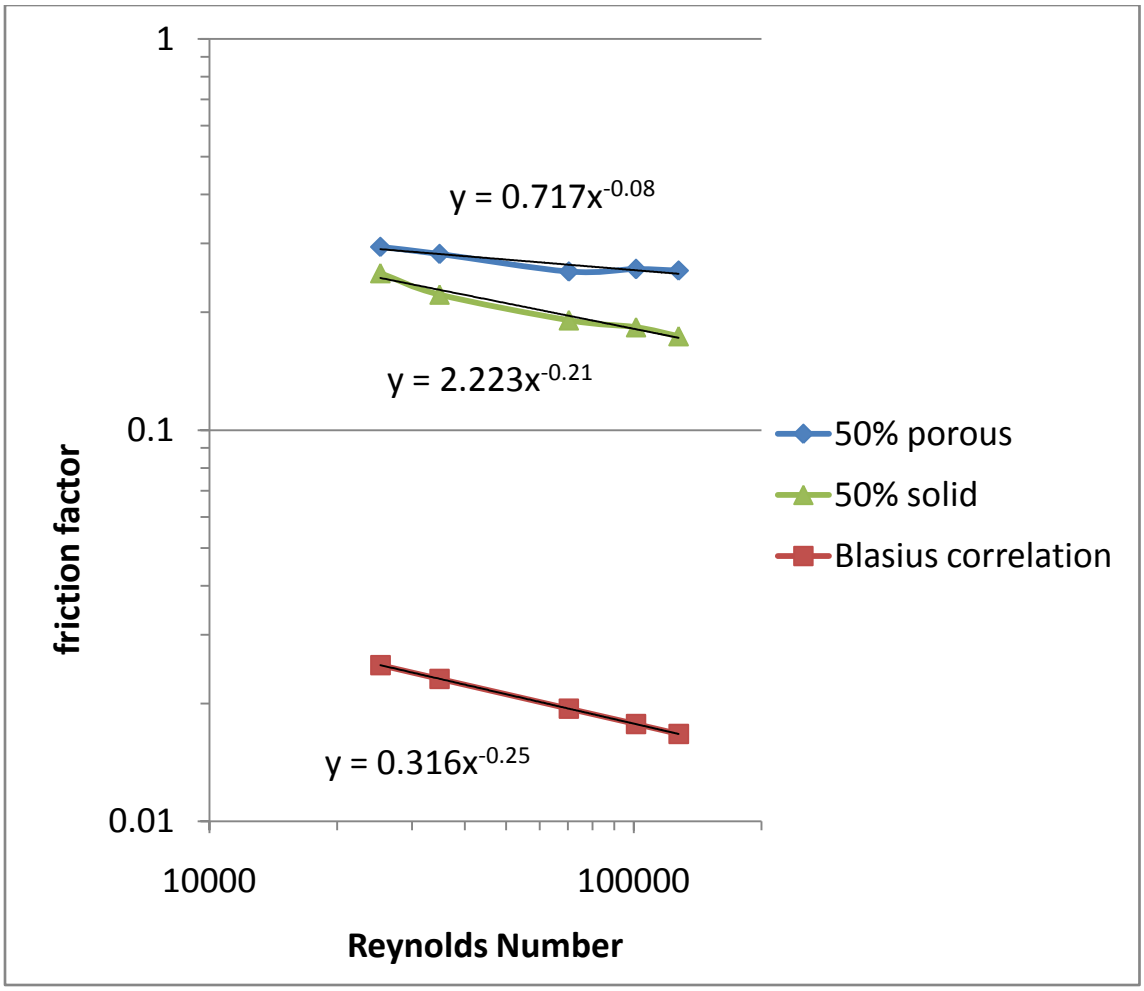

Figure 23: Friction Factor for Solid and Porous Pins

It can be seen from the figure that the friction factor is consistently higher for porous pins as compared to solid pins of the same dimensions. These results are opposite of what was found by Ko who determined that the friction factor through porous baffles was always lower than that of solid baffles. This increased friction factor resulting from the porous pins may be a result of a significant increase in the friction drag on the flow through the test section that occurs because of the large surface area contacted by the flow through the porous pins.

One trend that can be observed from Figure 23 is that the deviation of the porous pin friction factor from the solid pin friction factor increases as the Reynold's number is increased. For lower flow rates, the friction factor for the porous pins is closer to the friction factor of the solid pins. Although Kim et al (2000) tested at much lower flow rates (approximately Re = 200-2000), he observed what is possibly the same trend observed in this study. At very low flow rates, the porous fins exhibited a lower friction factor. As the flow rate was increased, the trend was reversed and the porous fins began to exhibit a higher friction factor as compared to the louvered fins. These trends may imply that for very low flow rates, the pressure drag dominates the total drag around each pin, thereby resulting in a higher pressure drop for the solid pins. As the flow rate is increased, however, the friction drag begins to dominate, resulting in an increasing pressure drop for the porous pins.

Local HTC Data and Results

Average endwall HTC values were obtained for porous and solid pins with Reynold's numbers between 25000 and 130000. Figure 24 shows a plot of the endwall average HTC vs. Reynold's number compared to the Dittus-Boelter correlation for a smooth channel.

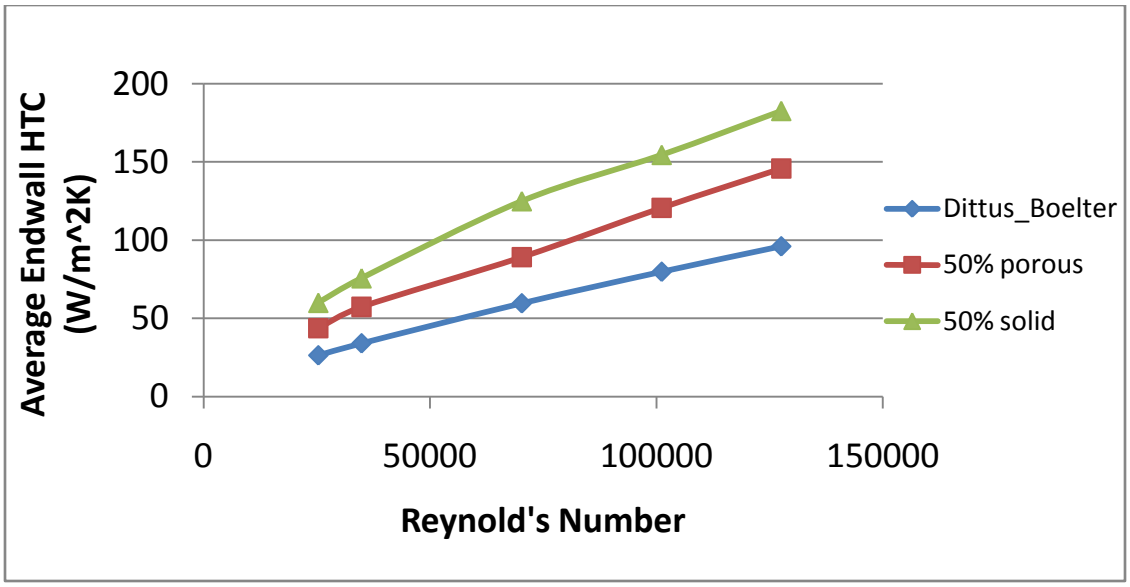

Figure 24: Average Endwall HTC's for Solid and Porous Pins Compared to Dittus-Boelter

As expected, it can be seen from this plot that the solid pins provide the most heat transfer enhancement, followed by porous pins, and then by a smooth channel. This is the same trend that was found by Ko et al (2003) when he also compared porous and solid baffles to a smooth channel. It is also apparent from the figure that both the solid and porous data begins to diverge more from the baseline case as the Reynolds number is increased.

Local HTC plots were determined for each of the various cases tested. Figure 25 compares the local HTC plots for porous and solid pins at a Reynold's number of 130000.

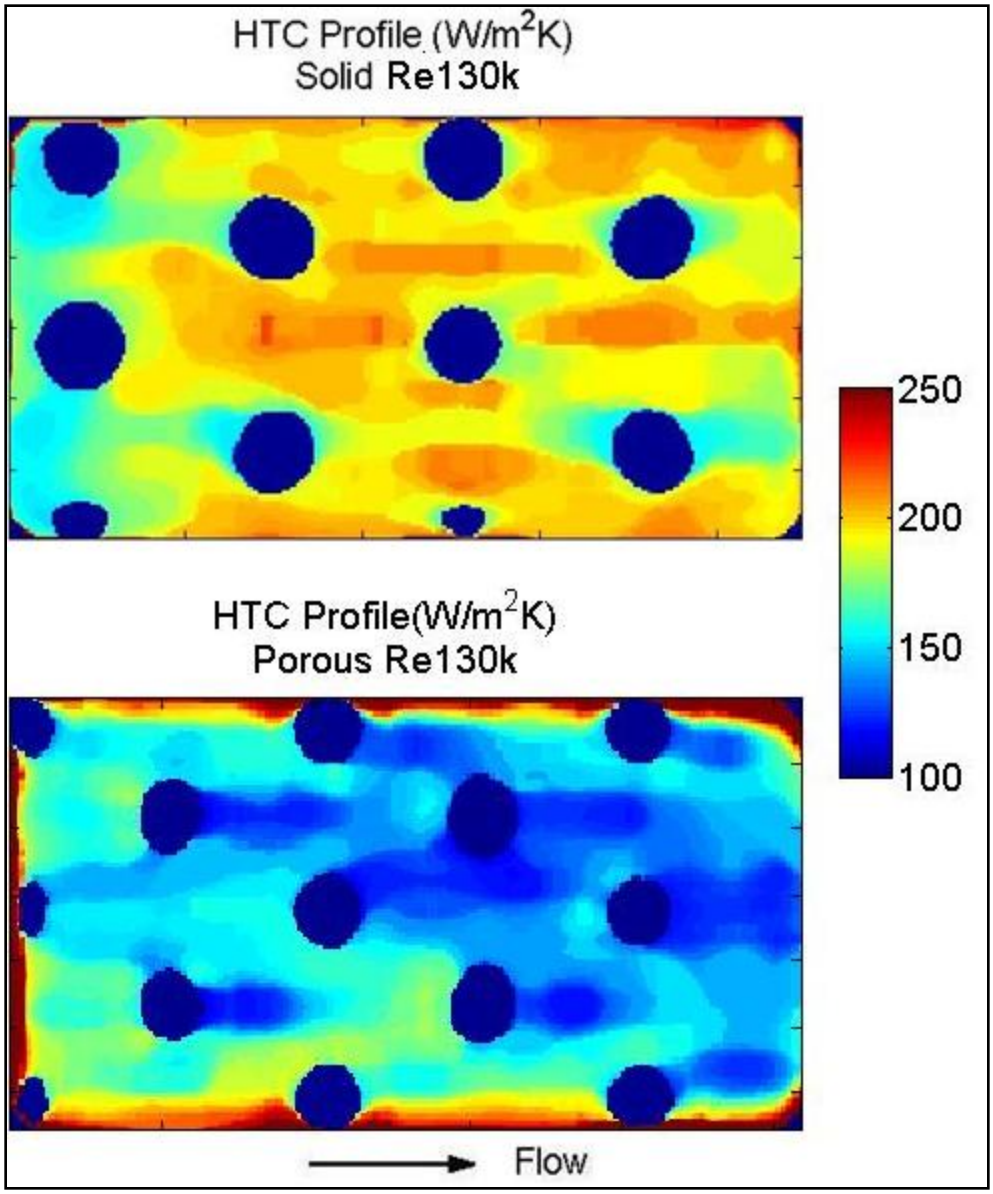

Figure 25: Local HTC Plots for Porous vs. Solid Pins: Re130000

First, it is apparent from this figure that the overall local HTC's throughout the plots are much higher for the solid pins. This agrees with the pressure data discussed earlier, which illustrated that the flow through the porous pins was restricted as compared to the flow through

the solid pins. This is most likely a result of the high friction drag that occurs through each pin, slowing the flow down and consequently decreasing the local HTC values.

Another difference between the porous and solid HTC plots is the locations of minimum local HTC. Immediately behind the rear surface of the solid pin is a region of low HTC where the velocity of the flow is significantly reduced in the wake of the pin. This region of low HTC directly behind the pin does not occur with the porous pins but is actually replaced by a region of relatively high HTC. This shows that a small amount of the flow is passing through the porous pin, slightly enhancing the HTC in the recirculation zone.

Approximately one pin diameter downstream of the low HTC region seen in the solid pin array is a region of high HTC where the wake reattaches and the velocity of the flow is increased as the flow is forced between the next two pins. A similar region of high HTC was found between pins in the porous array, showing that the flow pattern around the porous and solid pins is similar in this region.

Another trend that can be observed from Figure 25 is that the distribution of HTC's across the endwall does not appear to be more even with the porous pins, as was initially expected. For the higher flow rates used in this study, it appears that there is just as broad a range of local HTC's across the endwall with porous pins as there is with solid pins. As the flow rate is decreased, however, this trend appears to change as the distribution of local HTC's from the porous pins begins to become more even across the surface of the endwall. Figure 26 shows the local HTC plot for solid and porous pins at a Reynold's number of 25000.

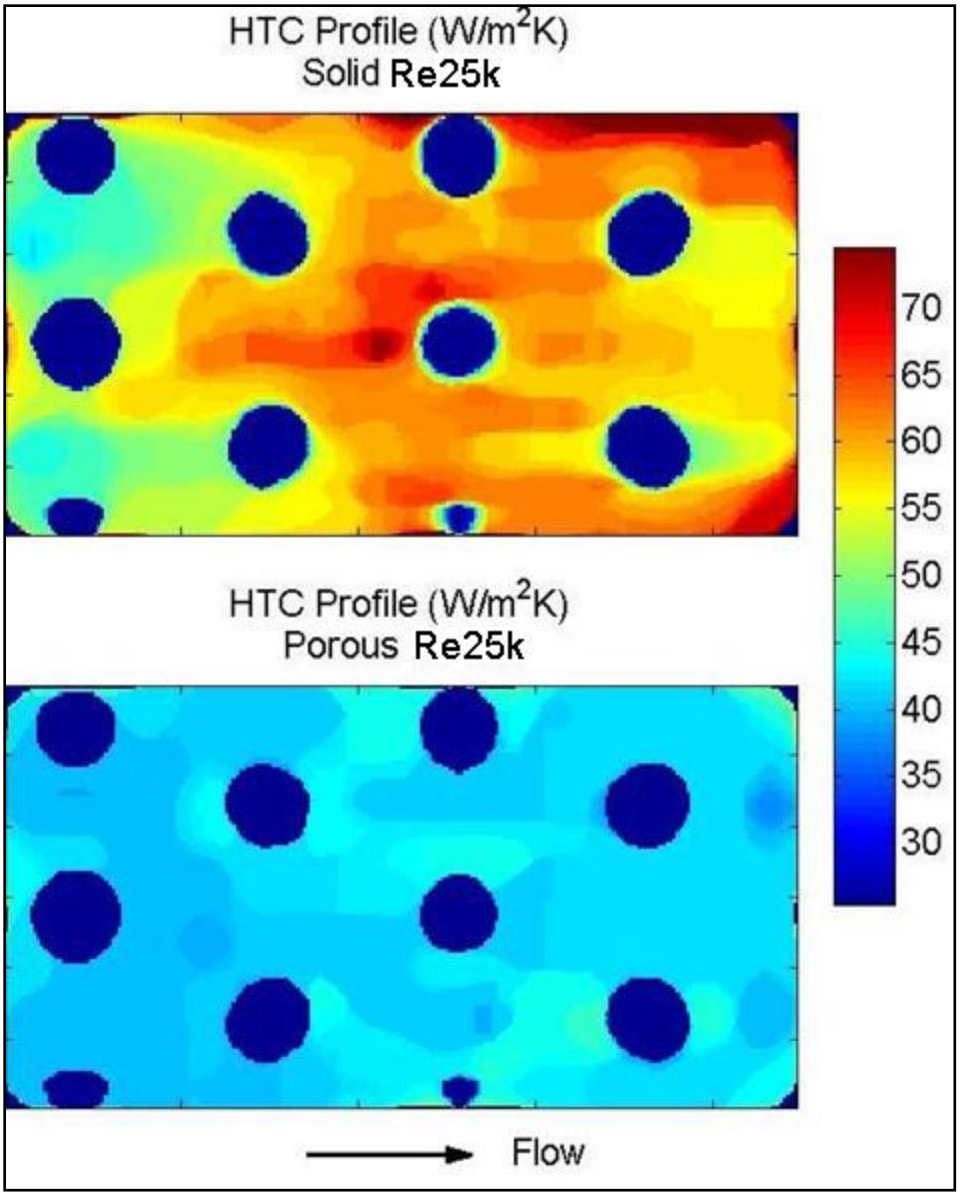

Figure 26: Local HTC Plots for Porous vs. Solid Pins: Re25000

Note from this figure that for the porous pins at this relatively low flow rate, the local HTC's only range from approximately 40-47 W/m^{2}K. At the same flow rate, the local HTC's for the solid pins range from approximately 46-64 W/m^{2}K. From the friction factor data discussed

earlier, it was found that for these lower flow rates, the pressure drop through the bank of porous pins was closer to that of the solid pins. As the flow rate increased, however, the porous pin pressure drop began to increasingly deviate from that of the solid pins. This suggests that as the flow rates are lowered, the porous pins may become more beneficial, resulting in a similar pressure drop to solid pins and a more even distribution of local HTC's.

Correction for Lateral Conduction

In calculating the local HTC data shown above, it was assumed that the heat flux conducted through the heater traces normal to the flow direction. In reality, however, some of the heat flux can be conducted laterally through the heater, especially near the contact area between the pin and heater surfaces. It was necessary to correct for this lateral conduction in the local HTC plots, at least once, to determine if this had a significant effect on the results shown above. The lateral conduction correction was done by determining the temperature difference between each pixel, which is what would drive any heat conduction in the lateral direction. Knowing the thermal conductivity of the heater traces, the thickness of the traces, as well as the spanwise and streamwise dimensions of each pixel, an energy balance could be done per pixel to find the amount of heat that conducts into a particular pixel laterally. This heat conducted laterally was then divided by the surface area of the pixel to determine the heat flux conducted into (or out of) that pixel. Finally, this laterally conducted heat flux could be added to the original heat flux calculated for that pixel and the corrected heat flux matrix was used to determine the corrected HTC values. Figure 27 shows a plot of the local HTC at a Reynold's number of 70,000 assuming

no lateral conduction compared to a plot of the local HTC correcting for lateral conduction. As you can see from the figure, there is no significant difference in the local HTC plots.

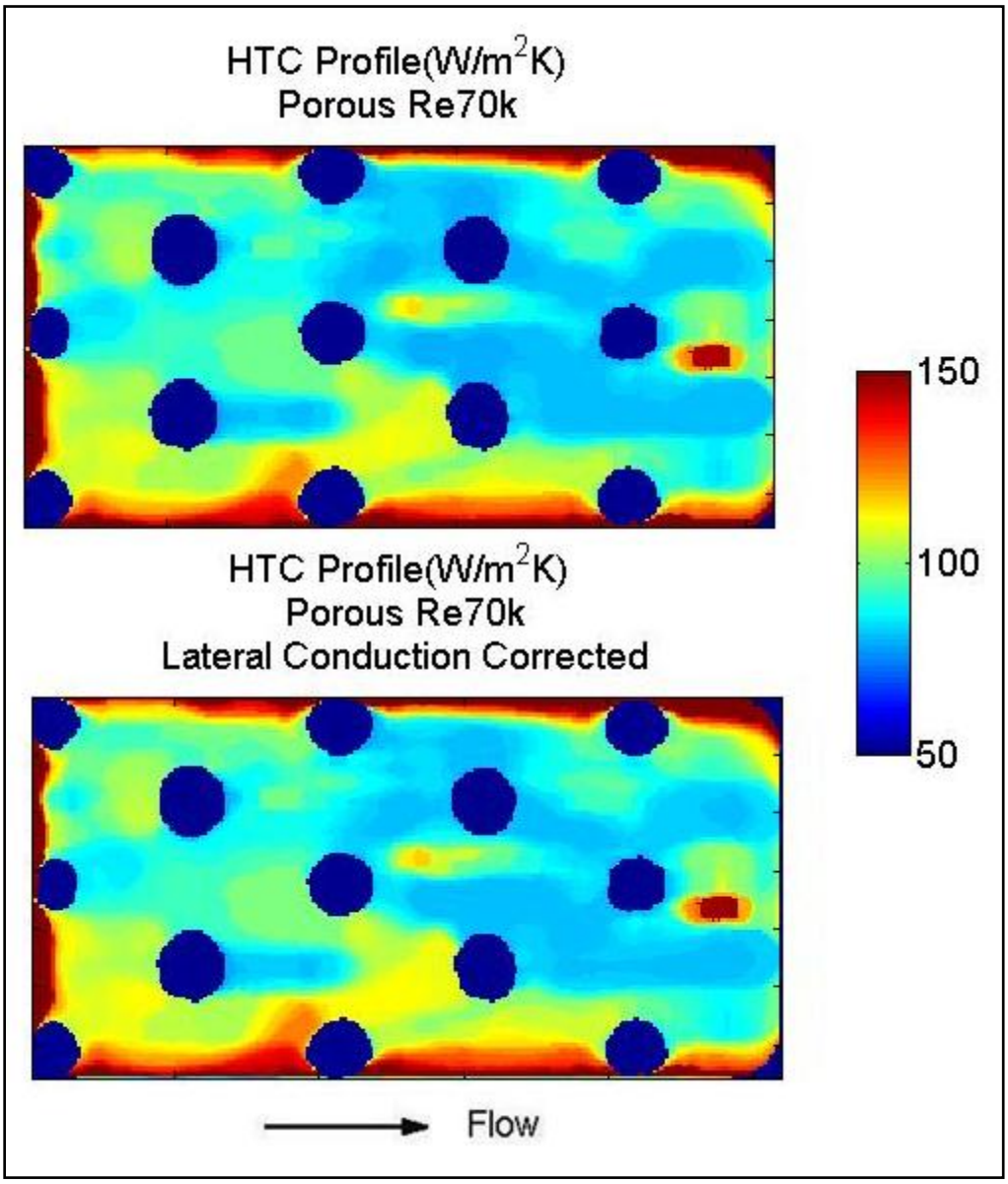

Figure 27: Local HTC Plot with Lateral Conduction Correction

It was found that the largest deviation in local HTC's resulting from the lateral conduction correction was approximately 1.2% for the porous pins and 2.4% for the solid pins. The average HTC was less than 1% higher for the porous pins and just over 1% higher for the solid pins. This data shows that the amount of lateral conduction through the heater is small and can be neglected without significantly altering the results.

Flow Visualization

Flow visualization tests were performed at very low flow rates using a fog generator. Although it was difficult to measure the flow rate using the available equipment, it was estimated that the flow for these tests was done at a Reynold's number of approximately 5000. This Reynold's number was calculated by using a pitot probe to measure the dynamic pressure across the entrance of the test section and then converting this data to a mass flow rate and then finally a Reynold's number, using the open hydraulic diameter. It was difficult to obtain local HTC data at this low flow rate because of the very low variations in the endwall temperature that resulted from the slow movement of the air through the test section. Figure 28 shows a picture of the flow visualization test.

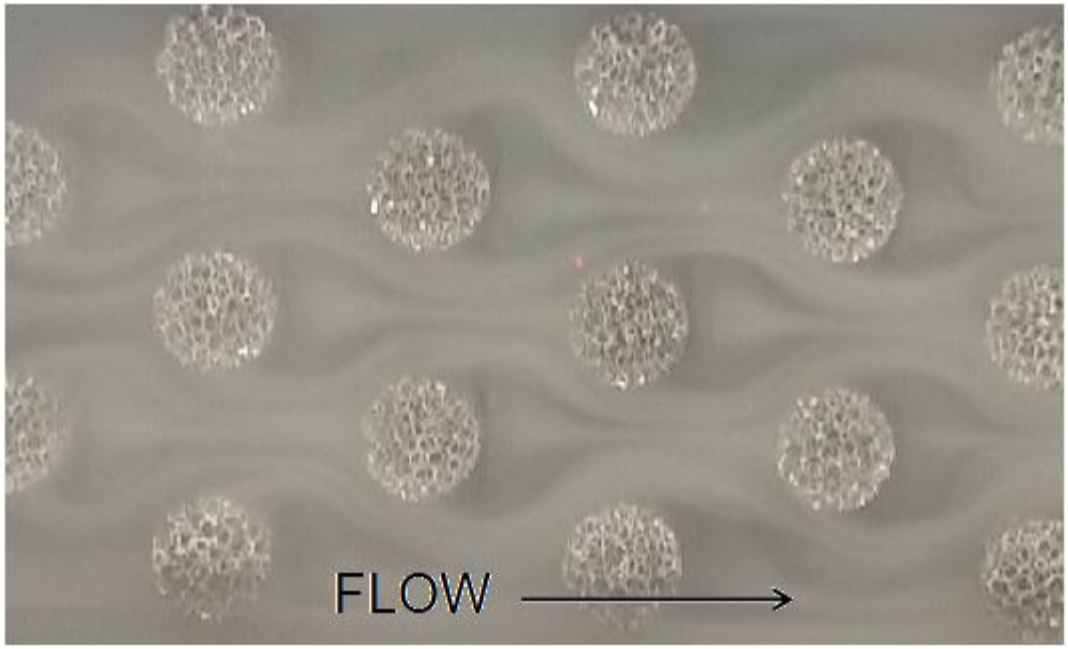

Figure 28: Flow Visualization Test (Re ~ 5000)

This test clearly shows how the flow moves around and between each pin throughout the test section. The recirculation zone behind each pin is also clearly visible. One interesting feature can be seen directly behind the pin where it appears that a small amount of the flow passes through the pin and then re-connects with the main flow between each pin. This agrees with the local HTC plots which showed slightly higher local HTC's directly behind the porous pins rear surface as compared to the solid pins. The increased heat transfer at the rear surface of the pin is attributed to a small amount of the flow passing through the porous pin, however, at higher flow rates, it appears that the amount of flow actually passing through the pin is greatly decreased. Another feature that can be seen in the flow visualization picture is the region in between each pin (in the spanwise direction) where the flow is accelerated as it is forced to squeeze in between

the pins. This corresponds to the region of local maximum HTC seen on the local HTC plots where the increased flow results in a higher amount of heat transfer from the endwall surface.

Figure 29 shows another figure of the flow visualization test, zoomed in on only a few of the porous pins.

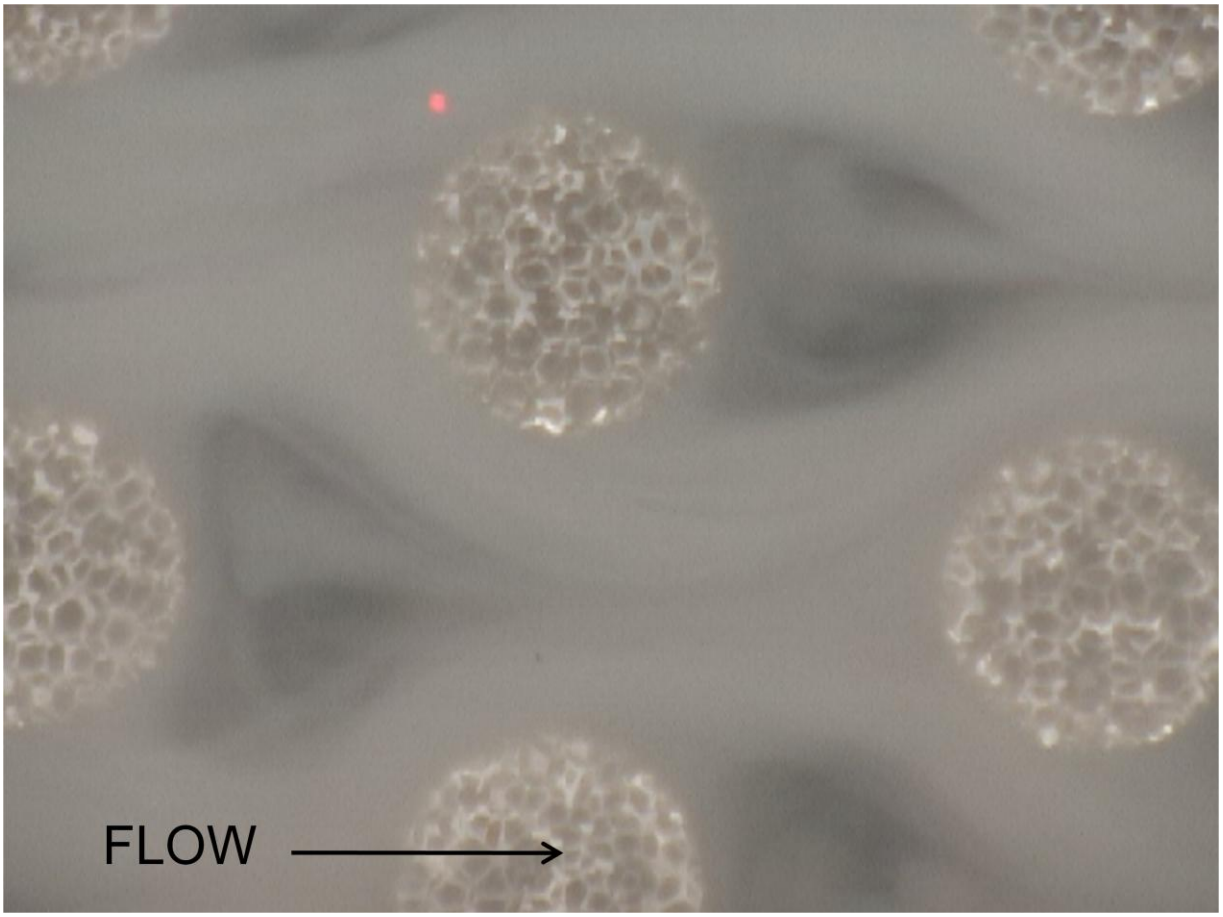

Figure 29: Close up View of Flow Visualization

Again, the recirculation zones directly behind each pin is clearly visible, corresponding to a region of low HTC behind the pin's rear surface. It also appears that the flow separates from the

pin surface relatively early which would cause a higher pressure drop through the test section. This helps to explain how the array or porous pins has a higher pressure drop through the test section than the array of solid pins.

Figure 30 shows another flow visualization test where both porous and solid pins were included in the same picture. Note that the porous pins are show in blue.

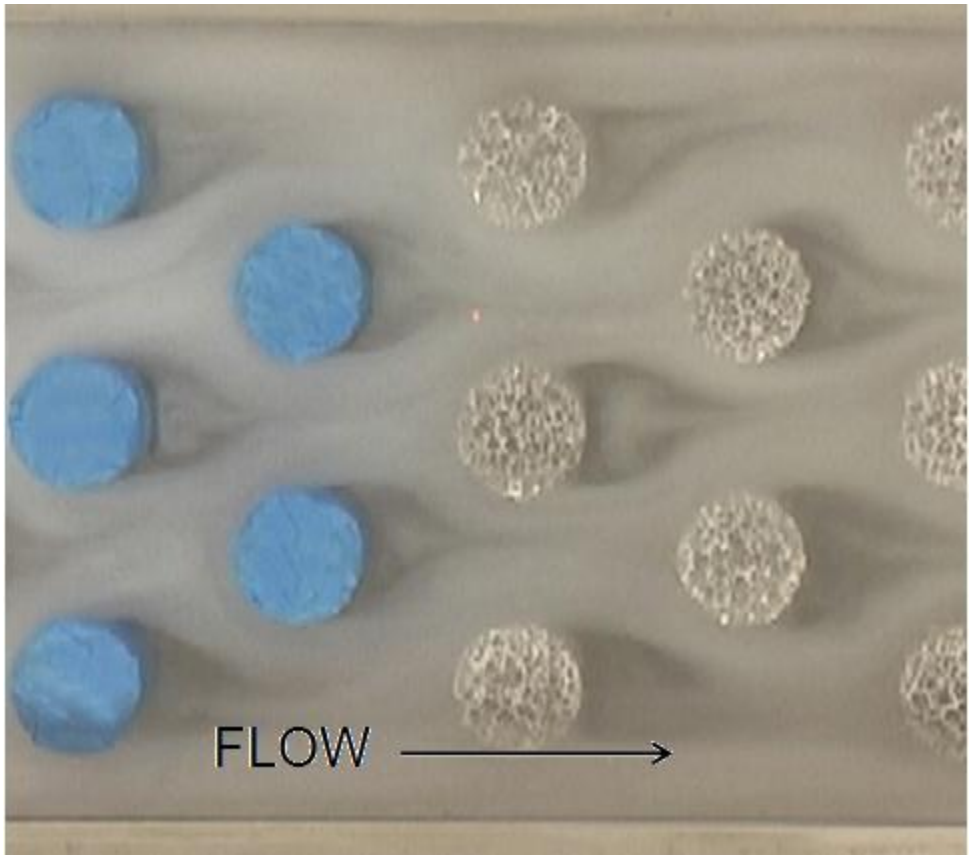

Figure 30: Flow Visualization (Porous and Solid)

It is interesting to notice from Figure 30 that the recirculation zones behind the porous and solid pins do not vary significantly. However, it does appear that the recirculation zones behind the

porous pins are slightly larger and the flow separates earlier than at the solid pins. This confirms what was found in the pressure measurements which showed that the pressure drop through the test section was consistently higher with the porous pins for the range of flow rates tested in this study.

Averaged HTC Data and Results

The matrices of local HTC data were averaged in both the spanwise and streamwise directions to demonstrate how the HTC's varied throughout the pin arrays. Figure 31 compares the porous and solid spanwise averaged HTC's for all of the flow rates that were tested in this study.

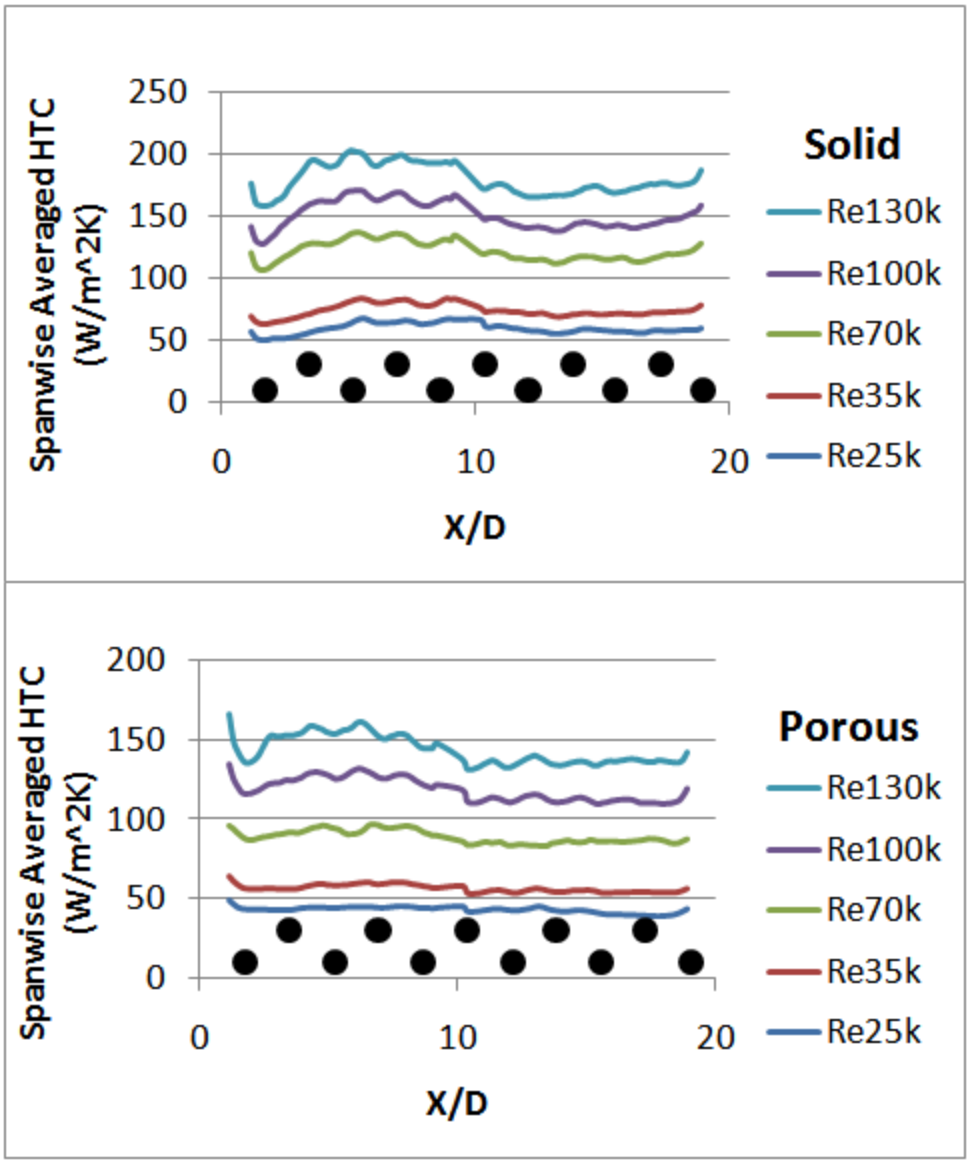

Figure 31: Spanwise Averaged HTC's for All Cases

The developing region before the first row of pins is evident in these plots by the rapid drop in the HTC at the very beginning of the channel. After the first row of pins, the HTC's then

begin to increase slightly and then level off by the 5th or 6th row of pins. This developing region occurred for both solid and porous pins and is similar to what was found by Chyu et al (1990).

Figure 32 gives a closer look at the spanwise averaged HTC's for the porous and solid pins at a Reynold's number of 130000.

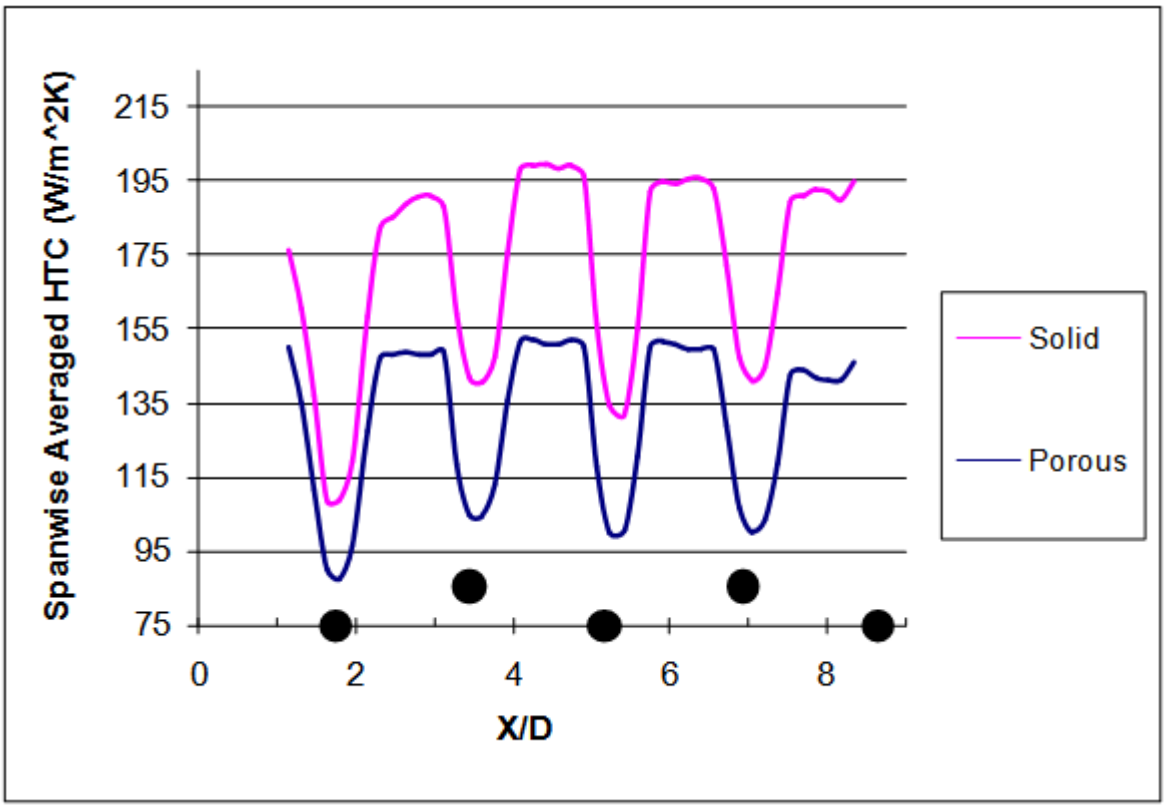

Figure 32: Spanwise Averaged HTC's (Re=130000)

The trend of this spanwise averaged plot is nearly identical to what was found by Chyu et al (1990). A local maximum occurs just before each pin followed by a local minimum at each pin. It is also interesting to note that the spanwise averaged trends between the porous and solid pins are identical.

Figure 33 shows the streamwise averaged HTC's for porous and solid pins, also at a Reynold's number of 130000.

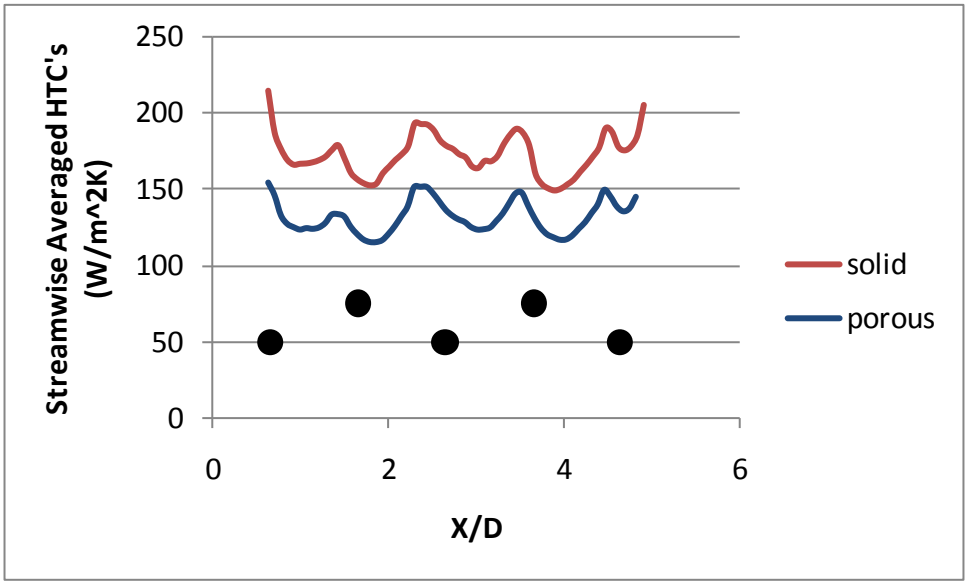

Figure 33: Streamwise Averaged HTC's (Re=130000)

Again the trends found here with the streamwise averaged plots are nearly identical to what was found by Chyu et al (1990) who found peaks between each column of pins. Also, similar to the spanwise average HTC's, the trends between porous and solid pins are identical.

Enhancement Ratios and Thermal Performance

A heat transfer enhancement ratio (h/ho) was determined by comparing the average endwall HTC to a baseline HTC calculated using the open hydraulic diameter of the test section

with the Dittus-Boelter correlation for smooth channel flow. Table 3 shows a table of the h/ho values for porous and solid pins.

Table 3: Heat Transfer Enhancement Ratios

Reynolds #	**Porous h/h_o**	**Solid h/h_o**
25000	1.66	2.28
35000	1.69	2.23
70000	1.50	2.10
100000	1.51	1.94
130000	1.52	1.90

As determined from previous data, the heat transfer enhancement is consistently higher with the use of solid pins. It is also observed for both porous and solid pins that the heat transfer enhancement slightly decreases as the Reynold's number is increased.

A similar ratio was determined for the friction factor, f/fo, again using the open hydraulic diameter of the test section with the Blasius correlation for smooth channel flow. Table 4 shows a table of the f/fo values for porous and solid pins.

Table 4: Friction Factor Ratios

Reynolds #	**Porous f/fo**	**Solid f/fo**
25000	11.73	10.05
35000	12.19	9.60
70000	13.10	9.83
100000	14.56	10.34
130000	15.30	10.39

This table verifies that the friction factor is significantly increased with the incorporation of porous pins into the test section. It is also evident that for the solid pins, the friction factor

ratio remains relatively constant as the flow rate is increased. For porous pins, however, the friction factor ratio continues to increase as the flow rate increases. For the range of Reynold's numbers used in this study (25000-130000) a 30% increase in the friction factor ratio was observed.

It is known that although the HTC's always increase with increasing Reynold's number, the pressure drop through the test section also increases. It is therefore necessary to determine a balance between the benefit of increased HTC's and the detriment of the significantly increased pressure drop. This comparison can be made by implementing Equation (4) to determine the thermal performance of each test, using the open hydraulic diameter as the baseline case.

$$\varepsilon = \frac{h/h_o}{\left(f/f_o\right)^{1/3}} \tag{4}$$

Figure 34 shows a plot of the efficiencies vs. the Reynold's numbers for each case tested in this study.

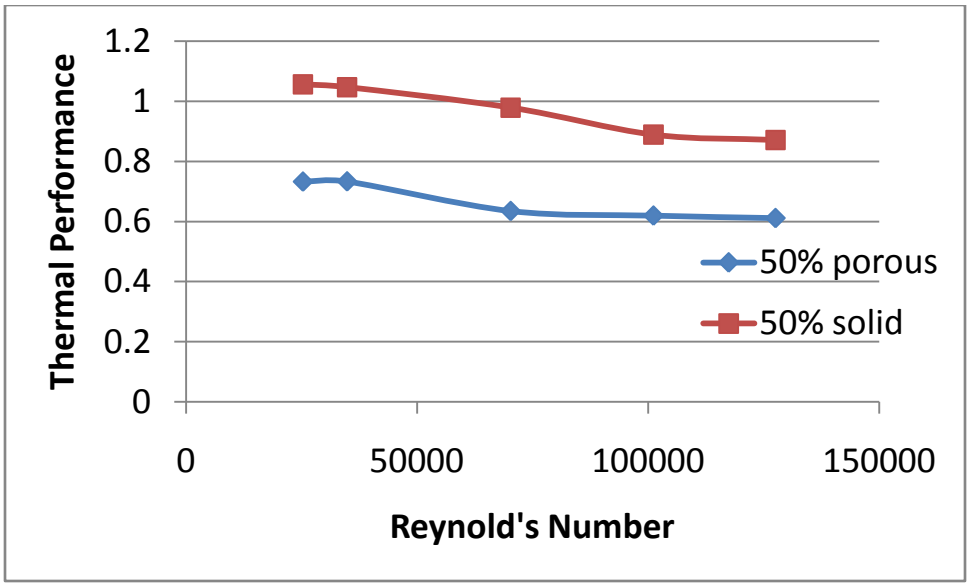

Figure 34: Thermal Performance of Porous and Solid Pins

As expected from the previous data, the efficiencies of the solid pins are consistently higher, ranging from 0.87 to 1.06. This implies that for the cases presented in this study, the solid pins prove to be a more effective means of heat transfer enhancement.

CHAPTER 5 – CONCLUSIONS

This study resulted in several important discoveries relating to the use of porous pin fins. It was found that for a large range of Reynold's numbers, the array of porous pins consistently resulted in a larger friction factor, and therefore greater losses, than a geometrically similar array of solid pins. This is attributed to the significantly increased friction drag that occurs as the air passes through the fibers of the porous pins. It also appears that the flow may be more drastically forced in directions anti-parallel to the main flow, causing a decrease in the overall velocity of the flow.

The heat transfer enhancement (h/ho) for the solid pins was higher for the lower flow rates and varied between approximately 190% and 230%. The heat transfer enhancement for porous pins was slightly lower, varying between approximately 150% and 170%. This decrease in heat transfer resulting from the porous pins is attributed to the overall decrease in flow velocity that results from the porous pins.

For the solid pins it was found that the friction factor ratio (f/fo) was relatively consistent between varying Reynold's numbers and averaged between 9.5 and 10.5, similar to results found in the literature. The friction factor ratio for porous pins was slightly higher for low Reynold's numbers and became increasingly higher as the Reynold's number was increased.

The local HTC plots indicated that the flow through the porous array of pins was being drawn into the pin from nearly all directions and passed through the rear surface of the pin. This resulted in regions of relatively low local HTC values between each pin in the spanwise direction but also regions of relatively high local HTC values immediately behind the pins. As known

from the literature, and confirmed in this study, these trends are nearly opposite to what occurs with a solid array of pins.

The thermal performance of the solid pins was found to be consistently higher than the thermal performance of porous pins, regardless of flow rate. The thermal performance of the solid pins varied from 0.87 to 1.06 while the thermal performance of the porous only fell between 0.61 and 0.73.

One of the motivations for conducting this research was the benefit of porous turbulators that has been discovered in studies performed by researchers such as Ko et al (2003) and Yang et al (2002). These benefits included high heat transfer enhancement compared to smooth channels, and more importantly, lower friction factors and more even endwall temperature distributions as compared to solid turbulators. It was found, however, that for porous pin fins, some of these benefits were eliminated, and the solid pins consistently resulted in higher heat transfer enhancement and lower friction factors. The higher heat transfer enhancement of the solid pins was expected and matches what has been found in nearly all of the research conduction on internal cooling with porous turbulators. The lower friction factor of the solid pins, however, was unexpected and is opposite to the trends that have been found in similar research using porous baffles. This dissimilarity is attributed to the significant geometrical differences that occur between the porous baffled test sections and the porous pin fin test section used in this study. In the baffled channels, the flow cannot move around the baffle as each baffle spans the entire spanwise width of the channel. Consequently, this forces the flow to either pass completely over the top of the baffle (with solid) or forces the flow to partially pass through the baffle and over

the top of the baffle (with porous). As was seen in the numerical study performed by Yang et al (2003), much of the flow did pass through the porous baffles, significantly decreasing the recirculation in the channel and thereby decreasing the friction factor. In the pin fin channels, however, the setup of the pins allows the flow to pass around each of the pins in the spanwise direction. As was seen in the flow visualization pictures, only a very small amount of the flow was forced through the porous pins. Most of the flow was diverted around the porous pins, similar to the flow field observed for a bank of solid pins. It was also observed that the flow around each porous cylinder separated earlier than the flow around the solid cylinders and the recirculation zones behind the porous pins appeared to be slightly larger. This is attributed to both types of drag that are increased as a result of the porous pins. The friction drag is increased as the flow passes around and through the porous pins because the surface area that the flow comes into contact with is increased due to the large amount of struts that make up the porous material. The form drag is also increased because of the sharp edges and angles that the flow has to maneuver through as it passes around and through the pin. Although these increases in drag would also exist through the porous baffles, the benefit of a significant amount of the flow passing through the baffle appears to outweigh these increases in the friction and form drag. As was confirmed by the flow visualization seen for both porous baffles and porous pins, the differences observed in the friction factor trends between the baffles and pins are attributed to the differences in the flow phenomena of the two geometries. The porous baffle setup forced a significant amount of flow to pass through the baffle. The porous pin setup allowed the flow to be almost completely diverted around the pins.

Because this study includes some of the first research in the area of porous pin fins, the results are difficult to compare with the literature. All of the data presented in this study, however, did confirm itself by comparing each of the various measurements, including the pressure data, local and average heat transfer data, and the flow visualization tests. Although this study presented a broad comparison between porous and solid pin fins, future research is essential to further classify how porous pin fins affect both the endwall heat transfer and friction factor through the cooling channel.

APPENDIX: COMPUTER CODES FOR TLC PROCESSING

** Note that this is only a sample of the code used for this project and is not exhaustive **

```
%crop images to equal sizes area

clear, clc, clear all;

%j=0; i=0;

%load images

c1=imread('porous_re18k.jpg');

%crop images

i=170:288;

j=118:340;

d1=c1(i,j,:);

%write images

imwrite(d1,'DAT_porous_re18k.jpg');




%TLC calibration

clear all, clc, close all;
```

```
%initialize variables

np=0, i=0, j=0, k=0, pp=0, dd=0, check=0;

%calibration pictures

np=25-6;

% all temperatures

T=[32 33 34 35 36 37 38 39 40 41 42 43 44 45 46 47 48 49 50 51 52 53 55 55 56];

%read images

pp=pp+1;

P=imread('cal_56_crop.jpg');

[h,s,v]=rgb2hsv(P);

HUE(:,:,pp)=h;

%Read Data

dd=dd+1;

D=imread('DAT_porous_re50k_mod.jpg');

 [h,s,v]=rgb2hsv(D);

DATH(:,:,dd)=h;
```

```
%create temperature matricies

[m,n]=size(HUE(:,:,1));

i=0;

for i=1:np

    TEMP(:,:,i)=ones(m,n)*T(i);

end

error=zeros(m,n);

for j=1:m

    for k=1:n

        hdat(:,1,1)=HUE(j,k,:);

        %make sure hue increases with temp, if not fix

        for check=2:pp

            if (hdat(check,1,1)<=hdat((check-1),1,1)) %<=if increasing t

                hdat(check,1,1)=(hdat(check-1,1,1)-hdat(check,1,1))*(+1)+hdat(check,1,1)+.0001;
%*+1,+.0001 for increasing

                error(j,k)=error(j,k)+1;
```

```
            check=check-1;
          end
      end
      tdat(1,:,1)=TEMP(j,k,:); tdat2(:,1,1)=TEMP(j,k,:);
      pict(j,k,1)=interp1(hdat,tdat,HUE(j,k,5));
%       dpict(j,k,1)=interp1(hdat,tdat,DATH(j,k,1));
      coeff=polyfit(hdat,tdat2,3);
      curve(j,k,:)=coeff;
   end
end
%average curve spot to 1 equation
jj=0;
for (jj=1:4)
   cm=mean(curve(:,:,jj));
   cm=mean(cm);
   avgcurve(1,jj,1)=cm;
```

```
end

%analize images and calib pics

for h=1:m

    for f=1:n

        pictpoly(h,f,1)=polyval(avgcurve,HUE(h,f,5));



    end

end




% convert temp data to h values; run after calibrate

%inlet and exit temps (deg C)

%*************CHECK TEMPERATURE ADJUSTMENT*************** (line 51)

Ti=22;

Te=Ti+3; %Re 39885

L=500*(1.22); %mm*pix/mm (L is in pixels)
```

```
 [i,j]=size(DATH(:,:,1));

%porous Re50k

qflux(1:i,1:j)=2427/0.9; %correction factor for space in b/w traces

 [md,nd]=size(DATH(:,:,1)); %image size

%h=0; f=0;

for h=1:md %g

    for f=1:nd

       if qflux(h,f)<=0

           tempprof(h,f,1)=0;

       end

%        if tempprof(h,f,1)>70

%            tempprof(h,f,1)=0;

%        end

    end

end

%h=0; f=0;
```

```
for h=1:md %get temperature information on desired images
    for f=1:nd
        tempprof(h,f,1)=polyval(avgcurve,DATH(h,f,1));%
    end
end
%calculate heat loss from average temperature
atemp=mean(mean(tempprof));
qloss=5.145*atemp-124.9;
qflux=qflux-(qloss); %heater wall flux W/m^2 - loss
TblkEQ=[(Te-Ti)/L Ti];
%plot temp profiles
% figure
% imagesc(tempprof), title('Temperature Profile; unfiltered'),imagemenu;
%filter image
tempprof=medfilt2(tempprof, [15,15])-0;
figure, imagesc(tempprof), title('Temperature Profile; filtered'),imagemenu;
```

```
% calculate local HTC's W/m^2K

h=0; f=0;

for f=1:nd

    for h=1:md

        htcprof(h,f,1)=qflux(h,f)/(tempprof(h,f,1)-polyval(TblkEQ,(f+0)));%(f+pixels from
beginning of heater)

    end

end

figure

imagesc(htcprof), title({'HTC Profile(W/m^2K)';'Porous Re50k'}), imagemenu;




%Spanwise averaging

stp=5; %to smooth out data

spavg=zeros(ceil((nd/stp)),1); spsm=zeros(ceil((nd/stp)),1);

pixig=0;
```

```
n=0; i=0; j=0;

jj=0; igarea=DATH(:,:,1);

for j=1:stp:nd

    n=0; jj=jj+1;

    for i=1:md

        if htcprof(i,j)<100 && htcprof(i,j)>30 %109

            spsm(jj)=htcprof(i,j)+spsm(jj);

            n=n+1;

        else

            pixig=pixig+1;

            igarea(i,j)=0;

        end

    end

        spavg(jj)=spsm(jj)/(n);

end

dia=25;
```

```
pxpm_st=1.22;

loc=xlsread('pin_locations_span.xls')*(17.5/25);

L=((1:jj)*((1/pxpm_st)/dia)*stp)+30*(1/pxpm_st)/dia;   %pixel* D/pix+ pixeloffset*D/pix

figure, plot(L,spavg,'x-',L,mean(spavg),loc,50,'ro'), title({'Spanwise Average';'Porous Re18k'})

counter=0;

sum=0;

for i=1:jj

    if spavg(i)>0

        sum=sum+spavg(i);

        counter=counter+1;

    else

    end

end

avg=sum/counter

cspavg(:,2)=spavg;

cspavg(:,1)=L;
```

```
% Streamwise averaging

stp=2; clear spavg, clear spsm %to smooth out data

spavg=zeros(ceil((md/stp)),1); spsm=zeros(ceil((md/stp)),1);

pixig=0;

n=0; i=0; j=0;

jj=0; igarea=htcprof(:,:);

for i=1:stp:md

    n=0; jj=jj+1;

    for j=1:nd

        if htcprof(i,j)<1900 && htcprof(i,j)>20 %109

            spsm(jj)=htcprof(i,j)+spsm(jj);

            n=n+1;

        else

            pixig=pixig+1;
```

```
            igarea(i,j)=0;
        end
    end
        spavg(jj)=spsm(jj)/n;
end
% loc_st=xlsread('pin_locations_stream.xls')*(17.5/25);
pxpm_sp=1.1;
L=((1:jj)*((1/pxpm_sp)/dia)*stp)+15*(1/pxpm_sp)/dia;   %pixel* D/pix+ pixeloffset*D/pix
figure, plot(L,spavg,L,mean(spavg)), title({'Streamwise Average';'TWEN rib C 50% Re106968 repeat'})
cstavg(:,2)=spavg;
cstavg(:,1)=L;
```

LIST OF REFERENCES

Chyu, M. K., Goldstein, R. J., (1990). "Influence of an array of wall-mounted cylinders on the mass transfer from a flat surface" Int. Journal of Heat and Mass Transfer. Vol. 34.

Chyu, M. K. (1999). "Heat Transfer Contributions of Pins and Endwall in Pin-Fin Arrays: Effects of Thermal Boundary Condition Modeling" Journal of Turbomachinery. Vol. 121.

VanFossen, G. J. (1981). "Heat Transfer Coefficients for Staggered Arrays of Short Pin Fins" American Society of Mechanical Engineers.

Ko, Kang-Hoon, Anand, N.K. (2003). "Use of Porous Baffles to Enhance Heat Transfer in a Rectangular Channel," . Int. Journal of Heat and Mass Transfer. Vol. 46, pp. 4191-4199.

Kim, S.Y., Paek, J.W., Kang, B.H. (2000). "Flow and Heat Transfer Correlations for Porous Fin in a Plate-Fin Heat Exchanger," Journal of Heat Transfer, Vol. 122.

Incropera, F. P. (2007). "Fundamentals of Heat and Mass Transfer." 6th Ed. Wiley & Sons. New Jersey.

Yang, Yue-Tzu, Hwang, Chih-Zong. (2002). "Calculation of Turbulent Flow and Heat Transfer in a Porous-Baffled Channel," Int. Journal of Heat and Mass Transfer. Vol. 46, pp. 771-780.

Chang, S.W., Yang, T.L., Huang, C.C., Chiang, K.F. (2008). "Endwall Heat Transfer and Pressure Drop in Rectangular Channels with Attached and Detached Circular Pin-Fin Array," Int. Journal of Heat and Mass Transfer. Vol. 51, pp. 5247-5259.

Farino, D. J., Hacker, J. M., Moffat, R. J., Eaton, J. K. (1994). "Illuminant Invariant Calibration of Thermochromic Liquid Crystals," Experimental Thermal and Fluid Science 9:1-12.

Ligrani, P.M., Oliveira, M.M., Blaskovich, T. (2003). “Comparison of Heat Transfer Augmentation Techniques,” AIAA Journal 41, No. 3.

Akansu, S.O. (2005). “Heat Transfers and Pressure Drops for Porous-Ring Turbulators in a Circular Pipe,” Applied Energy. Vol. 83, pp. 280-298.

Zhong Chen, Q.L., Flechtner, U., Warnecke, H.J. (1997). “Heat Transfer and Pressure Drop Characteristics in Rectangular Channels with Elliptic Pin Fins,” Int. Journal of Heat and Fluid Flow. Vol. 19, pp. 245-250.

Sahin, B., Demir, A. (2007). “Performance Analysis of a Heat Exchanger Having Perforated Square Fins,” Applied Thermal Engineering. Vol. 28, pp.621-632.

Sahiti, N., Lemouedda, A., Stojkovic, D., Durst, F., Franz, E. (2005). “Performance Comparison of Pin Fin In-Duct Arrays with Various Pin Cross Sections,” Applied Thermal Engineering. Vol. 26, pp. 1176-1192.

Jeng, T.M., Tzeng, S.C. (2006). “Pressure Drop and Heat Transfer of Square Pin-Fin Arrays in In-line and Staggered Arrangements,” Int. Journal of Heat and Mass Transfer. Vol. 50, pp. 2364-2375.